# Physics-based dynamic rupture models, fault interaction and ground motion simulations for the segmented Húsavík-Flatey Fault Zone, Northern Iceland

**Bo Li[1,2], Alice-Agnes Gabriel[3,1], Thomas Ulrich[1], Claudia Abril[4,5], Benedikt Halldorsson[4,6]**

[1]Department of Earth and Environmental Sciences, Ludwig-Maximilians-University, Munich, Germany.
[2]Physical Science and Engineering Division, King Abdullah University of Science and Technology, Thuwal, Saudi Arabia
[3]Scripps Institution of Oceanography, UC San Diego, La Jolla, USA.
[4]Division of Processing and Research, Icelandic Meteorological Office, Reykjavík, Iceland
[5]Department of Earth Sciences, Uppsala University, Uppsala SE-75236, Sweden
[6]Faculty of Civil and Environmental Engineering, School of Engineering and Natural Sciences, University of Iceland, Reykjavík, Iceland.

**Key Points:**

- Physics-based, observational constrained dynamic rupture scenarios of the Húsavík-Flatey Fault Zone reproduce historic earthquake magnitudes.
- We explore the effects of segmented fault geometry, hypocenter location, fault stress and roughness on rupture dynamics and ground motions.
- Our physics-based scenarios show magnitude consistent average attenuation relationships and match with regional ground motion models.

Corresponding author: Bo Li, bli@geophysik.uni-munechen.de

## Abstract

We present 3-D spontaneous dynamic rupture earthquake scenarios for the Húsavík–Flatey Fault Zone (HFFZ) in Northern Iceland. We construct three fault system models consisting of up to 55 segments of varying geometric complexity. By varying hypocenter locations, we analyse rupture dynamics, fault interactions and their associated ground motions and observational uncertainties in 79 scenarios. We use regional observations to constrain 3-D subsurface velocities and viscoelastic attenuation as well as fault stress and strength. Our models account for topo-bathymetry, off-fault plasticity and we explore the effect of fault roughness. Our spontaneous dynamic rupture scenarios can match historic magnitudes. We show that the fault system segmentation and geometry, hypocenter locations, initial stress conditions and fault roughness have strong effects on multi-fault rupture dynamics across the HFFZ. Breaking of different portions of the same fault system leads to varying rupture dynamics, slip distributions and magnitudes. All dynamic rupture scenarios yield highly heterogeneous near-field ground motions. We observe amplification from rupture directivity, geometric complexities, and amplification and shielding due to topography. We recover a magnitude-consistent attenuation relationship in good agreement with new regional empirical ground motion models. Physics-based ground motion variability changes with distance and increases for unilateral vs. bilateral rupture. Our study illustrates important ingredients for fully physics-based, regional earthquake scenarios, their respective importance for rupture dynamics and ground motion modeling and how they can be observationally constrained and verified. We entail that dynamic rupture scenarios can be useful for non-ergodic probabilistic seismic hazard assessment, specifically in data-limited regions.



## Plain Language Summary

The Húsavík–Flatey Fault (HFF) network is one of the seismically most active zones in Iceland, and hosted several historical earthquakes with magnitudes larger than 6. Its accumulated seismic moment could result in an earthquake of magnitude up to 7, posing a high seismic risk to the nearby community. In this study, we show earthquake scenarios accounting for multi-physics and regional geology. In addition to reproducing comparable historic magnitude events, we also vary the slipping fault geometry and hypocenter locations. We explore mechanically possible scenarios and the corresponding ground shaking. Our results show distinct effects of the fault geometry, rupture directivity and fault roughness on rupture dynamics, slip pattern and magnitude, and the heterogeneous ground shaking along and across the faults. The magnitude consistent attenuation relationship of our physics-based ground motion matches new empirical ground motion models, but shows varying ground motion variability with distance. Our study provides an overview of multiple rupture scenarios in the HFF region and suggests that an ensemble of physics-based scenarios can complement classical seismic hazard assessment methods to better characterize the hazard of tectonically and seismically complex regions, especially when historical data are limited and the attenuation relationships are poorly constrained.


## 1 Introduction

Iceland, the most seismically active region in Northern Europe, is located on the Mid-Atlantic Ridge, the divergent margin where the North American and the Eurasian Plates spread. The Tjörnes Fracture Zone (TFZ) is a transform zone located in North Iceland, where it connects the Northern Volcanic Zone with the northern segment of the Mid-Atlantic Ridge, the Kolbeinsey Ridge. The TFZ is one of the most seismically active regions in Iceland. It consists of three sub-parallel fault systems (Einarsson, 1991): the Húsavík–Flatey fault zone (HFFZ), a $\sim$ 100 km-long segmented right lateral strike-slip fault system located at the center of the TFZ; the Grímsey Fault Zone, an en-echelon

fault system located $\sim 40$ km NE of the HFFZ, with associated normal and strike-slip seismicity; and the Dalvík Fault Zone (DFZ), located ∼30 km SW of the HFFZ (Figure 1a). The fault segments of the HFFZ are aligned with regional tectonic deformation. It is the largest transform fault in the TFZ and accommodates 1/4 of the total plate transform motion, estimated as 19.4 mm/year (Metzger & Jónsson, 2014).

The HFFZ poses a high seismic risk to the town of Húsavík and nearby coastal communities in North Iceland. Húsavík is the second largest town in the area and an important touristic site, located directly atop the eastern segment of the HFFZ. Several large historical earthquakes have been associated with the HFFZ. The largest events are the 1755 M7.0 event and two M6.5 earthquake in 1872 (Stefansson et al., 2008). Metzger & Jónsson (2014) suggest that the seismic moment accumulated on the HFFZ since the last major earthquake in 1872 is equivalent to a potential imminent earthquake of magnitude 6.8 to 7. The seismic source model of Snaebjornsson & Sigbjornsson (2007), designed for hazard assessment, divides the HFFZ into three planar segments from west to east, two NW-SE striking segments, and one NE-SW oblique segment. Their assumed maximum potential earthquake magnitudes on each segment are $M_{\mathrm{w}}7.3$, $M_{\mathrm{w}}7.3$, and $M_{\mathrm{w}}6.5$, respectively.

In general, the seismic hazard in Northern Iceland is poorly constrained. Seismic studies in the area are challenging due to the mostly offshore location of the TFZ including the HFFZ. The Icelandic permanent seismic network (SIL) has recorded regional earthquakes since 1993 with stations mainly located on-land in North Iceland. The uneven distribution of the seismic stations increases the uncertainty of seismicity location parameters and introduces biases (Hensch et al., 2013). Additionally, strong earthquakes have not occurred in the TFZ during the operation time of the SIL network. The largest earthquake in the SIL catalog is an $M_{\mathrm{w}}6$ normal faulting event that occurred in 2020. The inherent limitations of the Northern Iceland earthquake databases pose it difficult to observationally constrain the required information for seismic hazard studies. Previous probabilistic seismic hazard analysis (PSHA) studies (Solnes et al., 2004; D'Amico et al., 2016) have thus used ground motion prediction equations (GMPEs) or ground motion models (GMMs) based on data sets from the Southern Iceland Seismic Zone (SISZ), an area that is tectonically and seismically "symmetric" to the TFZ relative to the plate separation vector (Einarsson, 2008; Panzera et al., 2016), but denser instrumented.

Importantly, earlier studies differ significantly in their estimates of the seismic hazard for the Húsavík area. Thus, a GMPE/GMM developed directly from physics-based dynamic rupture models, constrained with locally and regionally seismic and geological data, would be an important complement to assess the seismic hazard in the Húsavík region and Northern Iceland. Previous studies demonstrate the usefulness of deterministic earthquake models to improve ground motion predictions (e.g., Graves et al., 2011; Rodgers et al., 2020). While kinematic source descriptions do not guarantee physical consistency (P. M. Mai et al., 2016; Tinti et al., 2021), dynamic rupture simulations provide self-consistent models of how earthquakes start, propagate and stop and the associated seismic shaking (e.g., Guatteri et al., 2004; Schmedes et al., 2010; Gallovič et al., 2019). For example, Guatteri et al. (2003) show that high degrees of heterogeneity and complexity of dynamic source models have strong effects on near-fault ground motions. Dynamic rupture models can be used to better constrain kinematic source models for seismic ground motion modeling (e.g., Roten et al., 2012, 2014; Withers et al., 2019), and physics-based PSHA (Savran & Olsen, 2020). However, to model earthquake dynamics, choices about the required initial conditions including the preexisting state of stress and fault strength, as well as the fault geometries, are required (e.g., Ando & Kaneko, 2018; Tinti et al., 2021; Ulrich et al., 2022).

In this study, we develop a suite of 3D spontaneous dynamic earthquake rupture scenarios, based on varying levels of fault geometrical complexity and segmentation and varying hypocenter locations. We account for regional 3D subsurface structure, bathymetry

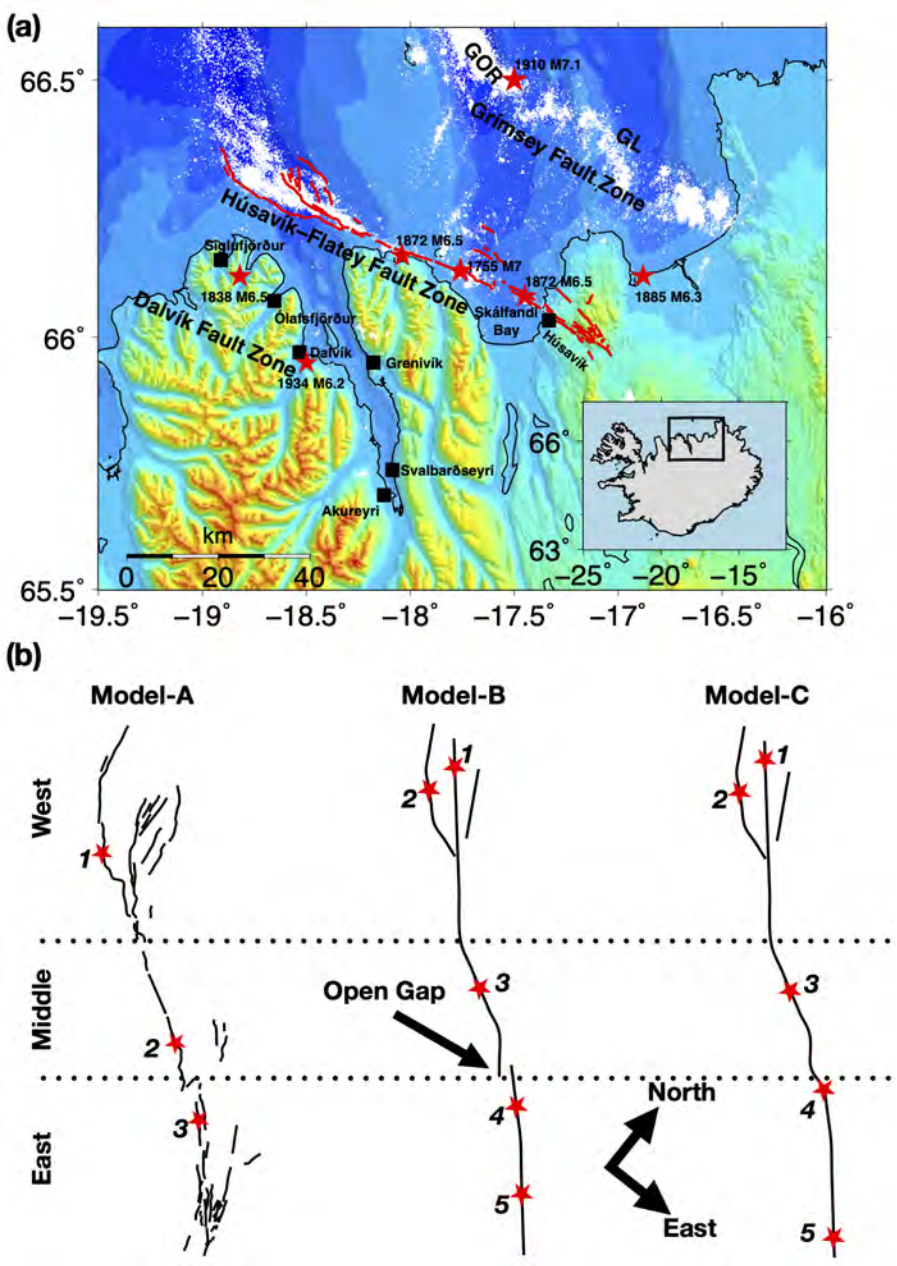


**Figure 1.** (a) Map of the Tjörnes Fracture Zone (TFZ). White dots show relocated earthquakes from 1993 to 2019 (Abril et al., 2018, 2019) and red stars mark the locations of historic large earthquakes (Stefansson et al., 2008). The red lines show the complex segmented fault traces of the Húsavík–Flatey fault zone (HFFZ) (Halldórsson, 2019) (Magnúsdóttir & Brandsdóttir, 2011; Magnúsdóttir et al., 2015; Hjartardóttir et al., 2016). The black squares mark the locations of major towns. The inset shows a map of Iceland, with the black box indicating the zoomed-in study region. (b) Fault geometry models used in dynamic rupture simulations. The black solid lines are the fault traces. Stars show the varied epicenter locations (hypocenters are at 7 km depth), with the index numbers identifying each rupture scenario. The dashed lines divide the HFFZ into the western, central, and eastern sections. The complex Model-A is traced in the map.

and topography, viscoelastic attenuation, the possibility of nonlinear fault zone plasticity (off-fault yielding), and fault roughness. We investigate complex fault system interaction, in terms of co-seismic dynamic and static stress transfers, and evaluate the potential for rupture cascading across the HFFZ. We systematically analyze the synthetic ground motions and identify amplification patterns due to rupture directivity, fault geometric complexity, and topography. We show that spontaneous dynamic rupture scenarios can match historic magnitudes and empirical ground motion models when informed by regional observations. Fully physics-based scenarios reveal more ground motion variability than typically captured in empirical approaches. Fault geometry, initial fault stress and strength are governed by dynamic trade-offs which are difficult to foresee without performing dynamic rupture simulations. Segmentation and complexity of fault geometry and differences in rupture dynamics, do not necessarily change distance-averaged ground shaking levels but change the physically plausible maximum magnitude and near-field shaking levels.

## 2 Model setup

### 2.1 Fault Geometries and Subsurface Model

We first construct a highly segmented model of the HFFZ (Figure 1b, Model-A), consisting of 55 partially intersecting, non-planar vertical faults, each also intersecting with the complex bathy-topography of the free surface. We integrate data from high-resolution bathymetry interpretation, offshore seismic reflection campaigns in Northern Iceland (Magnúsdóttir & Brandsdóttir, 2011; Magnúsdóttir et al., 2015; Hjartardóttir et al., 2016) and relocated seismicity (Abril et al., 2018, 2019) (Figure 1a). We assume vertical faults which is supported by the depth distribution of the recently relocated HFFZ-local seismicity from 1993 to 2019 considering the lateral variability of the crustal structure (Abril et al., 2018, 2019, 2021). Seismicity, initially located based on the recorded data by the permanent Icelandic - SIL network, has been relocated with a 3D tomographic velocity model of the study region. For the tomographic model by Abril et al. (2021), data from Ocean-Bottom Seismometers temporarily deployed in the TFZ has been used, which allows to illuminate the offshore areas of the TFZ and HFFZ, specifically. Our fault model agrees well with the horizontal extent of the relocated seismicity, and recent mapping of offshore faults and previous faults based on high-resolution bathymetry data (Brandsdóttir et al., 2005; Magnúsdóttir et al., 2015; Hjartardóttir et al., 2016).

We build a second fault system model, Model-B, that corresponds to a simplified and less segmented geometry. In Model-B, we acknowledge that the high complexity in mapped fault surface traces may not reflect the fault morphology at depth. This model is constructed by smoothing small-scale geometrical complexities of Model-A, such as sharp kinks, and merging multiple, short segments. Model-B reduces the HFFZ to four fault segments, two main faults and two secondary faults in the west (Figure 1b, Model-B). The main fault segment spans the whole HFFZ and can be divided into three units: the western, the central and the eastern sections. A $\sim 4$ km wide gap separates the central and eastern segments, which overlap over $\sim$1.5 km. This gap represents a prominent feature in the bathymetry in the middle of Skjálfandi Bay west of Húsavík, the Hóllinn seamount, that coincides with a sizeable lateral offset in the HFFZ (Magnúsdóttir et al., 2015).

We design a third model, Model-C, which is based on Model-B but closes the gap between the central and eastern segments. This model reduces the complexity of Model-B to three segments (Figure 1b, Model-C). By comparing the results of dynamic rupture simulations using Model-B versus Model-C, we are able to investigate the role of the fault system gap for co-seismic fault interaction and ground shaking in the HFFZ.

In all dynamic rupture scenarios, we limit slip at depth by smoothly tapering deviatoric stresses from 9 km to 11 km depth (see Section 2.3). This is motivated by the depth distribution of the relocated seismicity, which is limited, on average, to a depth of 10 km. We do not account for but discuss the effect of additional local variations of seismogenic depth. We embed all fault systems in the same 3D velocity model that was used for seismicity relocation (Abril et al., 2019, 2021) and use attenuation factors $Q_s = 50V_s$ ($V_s$ in km/s) and $Q_p = 2Q_s$, following the empirical relations in Olsen et al. (2009).

### 2.2 Numerical method and model discretization

We perform 3D earthquake dynamic rupture and seismic wave propagation simulations using the open-source software SeisSol (`https://github.com/SeisSol/SeisSol`). We ensure accurate analysis of seismic ground motions up to frequencies of at least 1 Hz by adapting SeisSol's mesh resolution to the 3D velocity model. Based on the (conservative) numerical analysis presented in Käser et al. (2008), SeisSol requires ∼2 elements for highly accurate resolution of the shortest wavelengths using a numerical scheme with basis functions of polynomial degree 7, and ∼4 elements with basis functions of polynomial degree of 4. We verify that our meshes resolve the seismic wavefield up to frequencies of 2.5 Hz in the vicinity of the highly resolved fault systems.

We discretize the 300 km × 284 km × 200 km modeled domain into statically adaptive unstructured tetrahedral meshes, locally refined around the fault network and near the surface topo-bathymetry. The mesh size is coarsened gradually away from the HFF system, from 150 m on-fault resolution to a maximum high-order accurate element size of 5 km. The 150 m fault discretization is effictively discretized by a maximum distance of 25 m when using fifth-order accuracy in space and time (i.e., basis functions of polynomial order $p = 4$, (Pelties et al., 2014)), which is sufficient to resolve the *minimum* cohesive zone width of $\sim 220\ m$ and its average width of $\sim 335\ m$ measured during dynamic rupture propagation (Day et al., 2005; Wollherr et al., 2018).

Our 3D structural model incorporates topography and bathymetry data from GeoMapApp (`www.geomapapp.org`)/(Ryan et al., 2009) at a resolution of ∼244 m, which is discretized at a resolution of at least 1 km everywhere in the model domain, and locally much finer. The resulting meshes have ∼27 million elements and require ∼15 hours computational time using 960 cores of the supercomputer SuperMUC-NG for one simulation.

### 2.3 Initial stress and fault friction

We pre-stress the geometrically complex networks of non-planar vertical and partially intersecting faults of our HFFZ Models-A, -B, and -C with a laterally homogeneous regional stress field. We constrain a regional 3D stress tensor from seismo-tectonic observations combined with physical assumptions on fault fluid pressurization and the Mohr-Coulomb theory of frictional failure, following Ulrich, Gabriel, et al. (2019). We also explore the effect of observational stress state uncertainties.

Our pre-stress and relative fault strength are fully defined by only four parameters:

1. the orientation of the regional maximum horizontal compressive stress $SH_{\max}$;
2. the stress shape ratio $s2_{\text{ratio}} = (s_2 - s_3)/(s_1 - s_3)$ with $s_1 > s_2 > s_3$ being the principal stress magnitudes;
3. the depth variation of the intermediate principal stress magnitude, here assumed as a function of the confining stress times $1-\gamma$. $\gamma$ is the ratio of the fluid pressure $P_{fluid}$ to the background lithostatic stress $\sigma_{zz} = \rho_{rock} g z$.

$\gamma = \rho_{water}/\rho_{rock} = 0.37$ corresponds to a hydrostatic stress state assuming a 1D rock density of 2670 $kg/m^3$ and higher $\gamma > 0.37$ correspond to fluid overpressurized stress states;

4. the maximum pre-stress ratio $R_0$. The relative pre-stress ratio $R$ is the ratio of fault stress drop and breakdown strength drop, and can be expressed as $(\tau - \mu_d\sigma'_n)/((\mu_s - \mu_d)\sigma'_n)$, in which $\tau$ is the shear stress on the fault, $\mu_s$ and $\mu_d$ are the static and dynamic friction coefficient, and $\sigma'_n$ is the effective confining stress. $R_0 = 1$ indicating a critical prestress level on all optimally-oriented faults (Aochi & Madariaga, 2003).

We follow Ziegler et al. (2016), who infer $SH_{\max} = 155 \pm 22°$ clockwise from north and $s2_{\text{ratio}} \sim 0.5$, from borehole breakouts, drilling induced fractures, earthquake focal mechanism inversion, geological information and overcoring measurements. This is consistent with a previous study by Angelier et al. (2004), who infer the orientation of the minor principal stress $\sigma_3$ to be 65°and $SH_{\max} = 155°$ clockwise from north, which is $\sim 50°$ deviation with respect to the 105° azimuth plate transform motion. We assume an Andersonian stress state, with $s_2$ vertical, which is supported by the inference of a nearly vertical intermediate principal stress by Ziegler et al. (2016), and is consistent with the overall transform plate motion. We generate a 1-D density model based on the averaged variability of our 3D P-wave seismic velocities with depth. We use that averaged 1D density model to calculate the depth-dependent confining stress, while the 3D velocity structure of Abril et al. (2021) governs seismic wave propagation.

Frictional yielding and dynamic slip across all faults is constrained by a linear slip weakening friction law (Ida, 1972; Andrews, 1976). Our assumed static ($\mu_{\text{s}}$ =0.55) and dynamic ($\mu_{\text{d}}$ =0.1) friction coefficients are consistent with laboratory-derived values for a large variety of lithologies (e.g. Byerlee, 1978; Di Toro et al., 2011). We find that the differences in geometric complexity between Model-A and Models-B & -C, impacts strongly on rupture dynamics across the segmented fault network and requires adapting the initial dynamic parameters to achieve comparable rupture scenarios depending on the fault geometry. We find that lower pre-stress ratios $R_0$ are dynamically unfavorable for rupture cascading across our segmented network of faults, while too high $R_0$ leads to unreasonable high stress drop, in agreement with previous dynamic rupture studies (Bai & Ampuero, 2017; Ulrich, Gabriel, et al., 2019).

All dynamic model parameters used for the varying geometry scenarios, which are presented in Sections 3.1-3.3, are summarized in Table 1. We adopt a maximum pre-stress ratio of $R_0 = 0.85$ for the most complex model (Model-A), which is closer to a critical stress state than our chosen $R_0 = 0.55$ in Models-B & -C. An optimally oriented fault plane would be critically loaded when $R_0 = 1$. A slightly shorter critical slip weakening distance $D_{\text{c}}$ in Model-A yields a smaller critical nucleation size required to initiate self-sustained rupture, e.g. by dynamic triggering (Day et al., 2005). In combination with the slightly increased pore fluid pressure ratio (Madden et al., 2022), Model-A parameters efficiently facilitate rupture cascading across its 55 short fault segments, producing earthquake scenarios comparable to Models-B & -C geometries and of historically plausible magnitudes.

In Section 3.4, we explore the sensitivity of rupture dynamics to dynamic model parameter choices, using the Model-C geometry. We vary $SH_{\max}$ between 135 ° and 170 ° clockwise from the north, the $s2_{\text{ratio}}$ between 0.4 and 0.9, $R_0$ between 0.45 and 0.65, and the fluid pressure ratio $\gamma$ between 0.55 and 0.70.

### 2.4 Off-fault plasticity

We account for the possibility of off-fault energy dissipation, by assuming a non-associated Drucker-Prager elasto-viscoplasticity rheology (Wollherr et al., 2018) within

| **Parameter** | **Model-A** | **Models-B & -C** |
|---|---|---|
| Static friction coefficient ($\mu_s$) | 0.55 | 0.55 |
| Dynamic friction coefficient ($\mu_d$) | 0.1 | 0.1 |
| Critical slip distance ($D_c$) within nucleation area (m) | **0.4** | **0.2** |
| Critical slip distance ($D_c$) outside nucleation area (m) | **0.4** | **0.5** |
| $SH_{max}$ | 155 | 155 |
| Seismogenic depth (km) | 10 | 10 |
| Maximum pre-stress ratio ($R_0$) | **0.85** | **0.55** |
| Pore fluid ratio ($\gamma$) | **0.75** | **0.6** |
| Stress shape ratio ($s2_{ratio}$) | 0.5 | 0.5 |
| Nucleation radius (km) | 1 | 1.5 |

**Table 1.** Dynamic rupture parameters for Model-A (Section 3.1) and Model-B (Section 3.2.1) and Model-C (Section 3.2.2 and 3.3). Fault network geometry specific differences are highlighted in bold.

the bulk of our model. Our implementation has been verified in community benchmark problems of the Southern California Earthquake Center (Harris et al., 2011, 2018). Our off-fault failure criterion is parameterized by two material properties, the internal friction coefficient and the bulk cohesion. The internal friction coefficient is set to be always equal to the fault static friction coefficient (=0.55). Considering the relatively slow local velocities, especially at shallower depths, we follow Roten et al. (2017)'s classification for weak rock. We set the 3D variable bulk cohesion to depend on the shear modulus $\mu$ as $C_{plast} = 0.0001\mu$ and $\mu$ varies spatially with the 3D velocity structure. A widely used rate-dependent viscoplastic relaxation mechanism is adopted to ensure convergence of the simulation results upon mesh refinement (Andrews, 2005; Duan, 2008; Dunham et al., 2011; Gabriel et al., 2013; Templeton & Rice, 2008; Xu et al., 2012). Its relaxation time $T_v$, over which stresses are relaxed to the yield surface and reach the inviscid stress state (Wollherr et al., 2018), also controls the effectiveness of plasticity and is set to 0.05 s. Off-fault initial stresses are set equal to the depth-dependent regional initial stresses loading the faults.

### 2.5 Rupture nucleation

Rupture initiation is prescribed smoothly in space and time by locally gradually reducing fault strength, $\mu_s$ (Harris et al., 2018). We initiate spontaneous dynamic rupture within an expanding circular area centered at a chosen hypocenter. The kinematic rupture initiation time $T$ is given by

$$T = \begin{cases} \frac{r}{0.7V_r} + \frac{0.081r_{crit}}{0.7V_r}\left(\frac{1}{1-(r/r_{crit})^2} - 1\right), & r <= r_{crit} \\ 10^9, & r > r_{crit} \end{cases} \quad (1)$$

where $r$ (km) is the radial distance to the hypocenter, $V_r$ is the initial forced rupture velocity, here set to 3800 m/s, and $r_{crit}$ is the radius of the nucleation zone. $r_{crit}$ is set to 1 km for Model-A, and 1.5 km for Model-B and Model-C, reflecting the varying pre-stress levels (see Table 1).

## 3 3D dynamic rupture scenarios

We first investigate the effects of fault geometry on rupture dynamics across the three HFFZ models. For each fault geometry, we generate unique rupture scenarios (3 for Model-A, 5 for Model-B, and 4 for Model-C) by varying the hypocenter locations (in-

dicated by stars in Figure 1b). Figure S1 shows that our Model-B and Model-C scenarios fit the scaling law of P. Mai & Beroza (2000) well when using the effective area. We omit a direct comparison with scaling laws for Model-A scenarios due to the high segmentation and coalescence of faults (Scholz et al., 1993). For this suite of 12 scenarios, we analyse the effect of fault geometry, rupture directivity, and topography on ground motion characteristics. We perform 4 additional scenarios adding fault roughness. Finally, we analyse the sensitivity of our dynamic rupture scenarios to the 4 key modeling parameters, the regional maximum horizontal compressive stress $SH_{\max}$, the stress shape ratio $s2_{\text{ratio}}$, the maximum pre-stress ratio $R_0$, and the fluid pressure ratio $\gamma$.

### 3.1 Dynamic rupture scenarios for a highly segmented Húsavík–Flatey fault zone geometry (Model-A)

We show three dynamic rupture scenarios across the most complex fault system (Model-A). The hypocenter locations are at 7 km depth but vary between the western (scenario A1), central (scenario A2) and eastern (scenario A3) sections of the HFFZ. We choose hypocentral locations based on the inferred epicenters of significant historical earthquakes such as the 1755 magnitude 7 (scenario A2) and 1872 magnitude 6.5 (scenario A3) events (Stefansson et al., 2008). There are no large historic events associated with epicenters in the West of the HFFZ (scenario A1). We note that the historical magnitudes are associated with considerable uncertainties. The spontaneously evolving dynamic rupture scenarios A2 and A3 with moment magnitudes $M_{\text{w}}6.91$ and $M_{\text{w}}6.50$, respectively, match the magnitudes of these historic earthquakes, which is an important result given we do not prescribe rupture propagation and arrest.

All three scenarios show complex rupture sequences. Rupture cascading across multiple fault segments leads to rupture front segmentation.3D subsurface impedance contrasts and free surface interactions cause additional rupture complexity such as healing due to reflected and interface waves (e.g., Dunham, 2005; Huang & Ampuero, 2011) and back-propagating rupture fronts (e.g., Beroza & Spudich, 1988; Idini & Ampuero, 2020). To illustrate the complexity of Model-A ruptures, we show in Figure 2 key characteristics of the A2 scenario that is associated with dynamic rupture of 13 fault segments of the complex fault system (Figure 2a). The rupture scenario features multiple dynamic triggering episodes (Figure 2b, and Movie S1) with irregular temporal progression in the moment rate release (Figure 2c).

The A2 scenario features localized, non-sustained supershear episodes, and dynamic complexity such as delayed or remote dynamic triggering and backward propagating rupture fronts (Figure 2b). Dynamic earthquake rupture takes first the form of a bilateral symmetrically propagating crack propagating away from the hypocenter at sub-shear/sub-Rayleigh rupture speed on fault segment 24 (F24). Rupture reaches the western edge of F24 at 1 s simulation time, and 2 s latter reaches the eastern edge. Rupture of F55 to the west is dynamically triggered, at 6-7 km depth, at about 3 s simulation time, and rapidly gains momentum on this more optimally oriented segment. A supershear daughter crack is then forming, ahead of the main crack. Next, F14, F17 and F16 are triggered to the west, which are fully ruptured at 7 s simulation time. After a 3 s long delay, associated with the first trough in the moment rate release, the segment F26 to the east of the nucleation region is dynamically triggered and fully ruptured. During this period, the parallel fault segment F25 does not break. Rupture continues further east with the dynamic triggering of the next segment to the east (F30). In the meantime, the rupture on F25 starts to nucleate but dies out quickly. After a short delay, the rupture jumps across a step over and breaks the segment F33 at a depth of $\sim$8 km. It then ruptures bilaterally across the whole segment at 13 s simulation time. This results in the rupture expanding updip and backwards, to the west. Then rupture on F25 to the west re-nucleates in the west again and breaks about 4/5 of that segment. While to the east, the rupture jumps through another step over, triggers rupture at the conjunction of F41 and F37,

then ruptures bilaterally, and finally breaks the whole segment of F37, F41 and F46 to the east. This is associated with the final peak of the moment rate function at ∼14 s. Scenario A2 results in the rupture of 13 segments over 17 s, and has a moment magnitude of $M_{\mathrm{w}}$ =6.91.

The three scenarios A1, A2, and A3 all involve different rupture sequences, different segments and yield different slip distributions (Figure 3a). The segments that spontaneously slip in scenario A3 also rupture in scenario A2. Generally, more slip is accumulated centrally on each of the ruptured segments. Maximum slip reaches ∼2.8 m, 4.2 m and 2.5 m for the three scenarios, respectively. While high slip is mostly modeled at hypocentral depth, larger shallow slip also appears, for example on segment F5, west of the nucleating fault (F7) in scenario A1. The fault segment (F55) west of the nucleating fault (F24) in scenario A2 hosts high slip across its entire seismogenic width, which is likely associated with local supershear rupture.

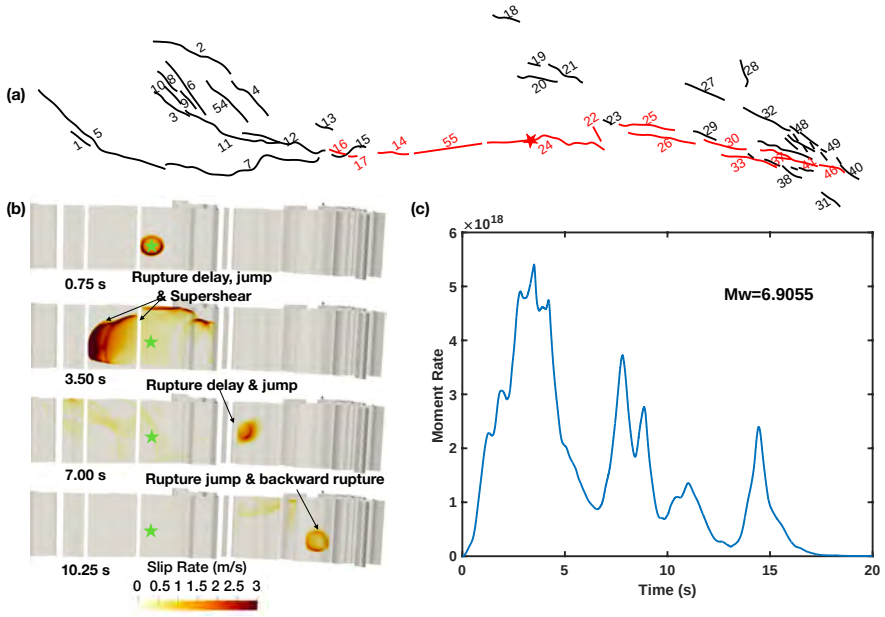


**Figure 2.** Dynamic rupture scenario A2 across the highly segmented Model-A fault network. (a) Map view of the fault traces for Model-A, with numbers denoting the fault segment index. The red lines mark the fault segments that ruptured in scenario A2. Some small segments in the east are not indexed. The red star marks the epicenter location. (b) Snapshots of the absolute slip rate, highlighting the complex rupture process at rupture times of 0.75 s, 3.50 s, 7.00 s and 10.25 s. Labels indicate noteworthy features of the rupture. Fault segments in the west of the HFFZ that did not rupture in A2 are not shown here. The green star mark the hypocenter location. (c) The time evolution of the modeled multi-peak moment rate release.

Maps of the resulting ground motions are shown in Figure 3 for all three rupture scenarios of the complex fault network Model-A. Spectral acceleration is defined as the rotation-invariant measure of pseudo-acceleration response spectral values on a wide range of oscillator periods (Boore et al., 2006)). We find heterogeneous ground shaking intensities across and along the fault system. Higher amplitude shaking localizes in the vicin-

ity of fault geometrical complexities, such as fault bends or gaps between segments, in the direction of rupture propagation. We relate this to rapid rupture acceleration and deceleration due to geometrically modulated locally different pre-stress conditions as well as barrier effects (e.g., Oglesby & Mai, 2012). Significant topographical features of the peninsula just south of the central HFFZ show amplified ground shaking consistently in all three models.

### 3.2 Dynamic rupture scenarios for simplified Húsavík–Flatey fault zone geometries (Model-B and Model-C)

To compare to the scenarios using the highly complex 55-segment fault network of Model-A, we next carry out dynamic rupture scenarios on more simplified and smooth fault geometries to investigate the effects of fault geometry and segmentation on rupture dynamics and the resulting ground motion characteristics. We pay special attention to the location of the Hóllinn seamount which coincides with a sizeable lateral gap in our geometry of the HFFZ in Model-B. This gap may potentially arrest propagating fault rupture on either side, and thereby curbing the maximum earthquake magnitude potential of the HFFZ and the corresponding near-fault ground motion amplitudes.

#### *3.2.1 "Open gap" between the middle and eastern HFFZ (Model-B)*

Multiple dynamic rupture scenarios are performed on the 4-segment geometry of Model-B, each of which with a different hypocentral location prescribed along the fault system. We refer to the epicenter indexes in Figure 1b as scenario identifiers. We use the model parameters summarized in the last column of Table 1. As detailed in Section 2.3, we use a slightly lower $R_0$, decreased $\gamma$, larger nucleation radius and larger $D_c$, to achieve comparable rupture dynamics to the more segmented Model-A geometry and to prevent sustained supershear rupture.

The simpler geometry of Model-B leads to dynamic rupture scenarios characterized by more simple rupture processes. The adapted dynamic rupture parameters render all faults in Model-B and Model-C scenarios dynamically stronger(Ulrich, Gabriel, et al., 2019) and less critically loaded. Rupture arrest and thus slip, however, is dominantly limited by the remaining complexities in the fault geometry. Importantly, in none of the explored scenarios is rupture able to jump across the gap between the middle and east segments. We note that the larger $D_c$ and lower pore fluid pressure required to achieve realistic slip, rupture speed and magnitudes likely impede dynamic triggering in comparison to Model-A scenarios.

Figure 4a and Movie S2 illustrates the simpler rupture process of scenario B3, representing an exemplary Model-B scenario. Rupture is nucleated at the center of the fault system and propagates bilaterally. Rupture to the east terminates when reaching the open gap at 7.2 s rupture time. This time coincides with the peak in the moment rate release (Figure 4b). The westwards rupture front breaks the entire middle segment, branches to the western segment, which is then ruptured integrally. This leads to a $M_{\mathrm{w}}$7.15 event, with a duration of 19 s. The earthquake rupture scenarios of Model-B which break the same segments have similar moment magnitude while their varying hypocenter locations modulate the accumulated fault slip distributions (Figure 5). For instance, scenarios B1 and B3 both rupture the western and middle segment of the main fault and have the same moment magnitude ($M_{\mathrm{w}}$7.15). But, the large slip asperity is shifted westwards in scenario B3 compared with scenario B1. Also in scenarios B4 and B5, the position of the high slip asperity depends on the hypocenter location.

Due to the smoother geometry of Model-B, the synthetic shake maps exhibit less spatial heterogeneity than those of Model-A. In addition, the scenarios result in ground shaking intensities that show very strong and expansive directivity effects. These are pro-

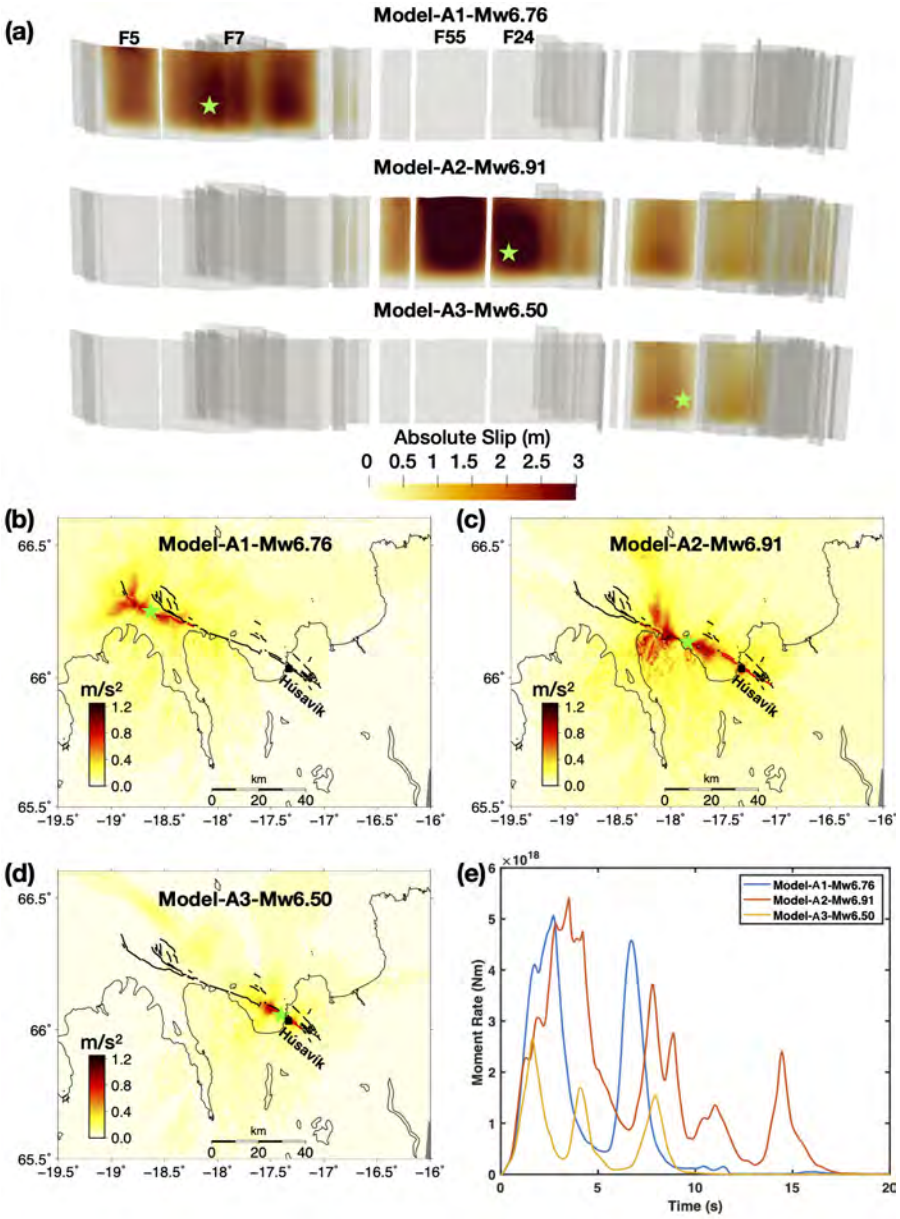


**Figure 3.** (a) Accumulated fault slip distribution and ground motion (spectral acceleration SA[1.0 s] in m/s$^2$) for three rupture scenarios using Model-A with varying hypocenter locations. Each scenario features distinct dynamics and involves different fault segments. The moment magnitudes of scenarios A2 ($M_{\mathrm{w}}$6.91) and A3 ($M_{\mathrm{w}}$6.50) resemble historical events with similar epicentres. (b-d) Ground motion maps ([SA 1.0s] in m/sˆ2). (e) Moment rate functions.

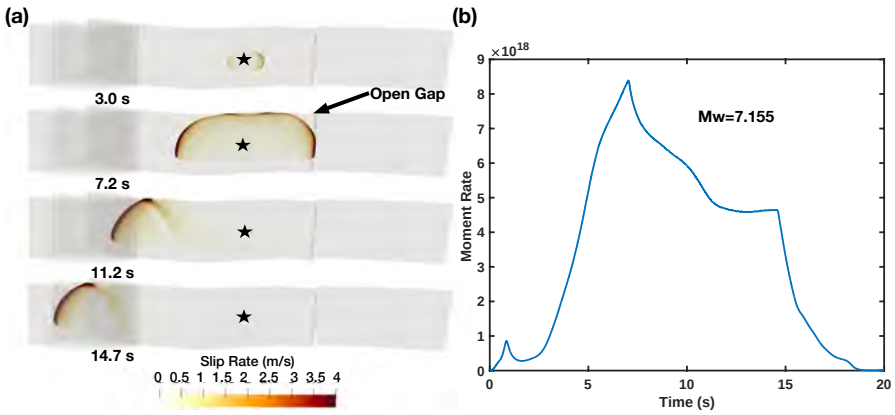


**Figure 4.** Overview of the simulated rupture propagation of scenario B3 using Model-B fault system geometry. (a) Snapshots of the absolute slip rate are shown at a rupture time of 3.0 s, 7.2 s, 11.2 s and 14.70 s. (b) Moment rate release of scenario B3.

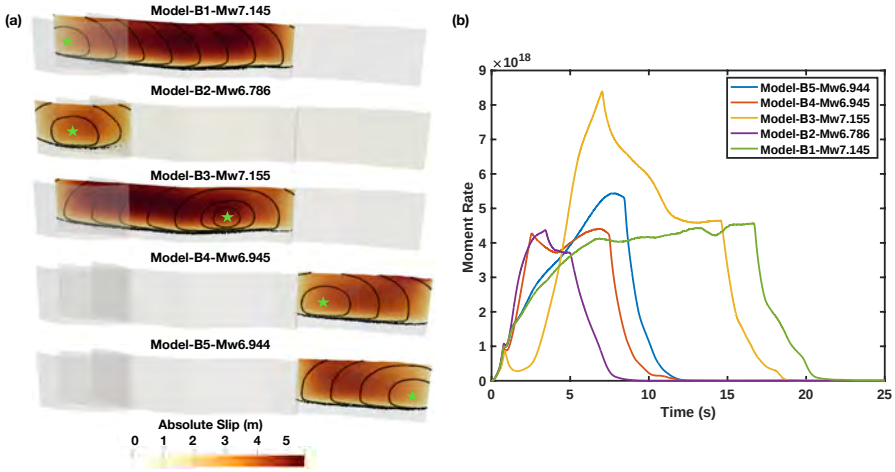


**Figure 5.** (a) Accumulated fault slip distribution of five rupture scenarios across Model-B, with different hypocenter locations. The green star marks the hypocenter location, at 7 km depth in all scenarios. The black contours are isochrones of the rupture time, with 2 s intervals. (b) Moment rate functions for the five rupture scenarios in (a). None of the explored scenarios are able to jump across the gap between the middle and east segments.

moted by the long and smooth faults and appear for both bilateral (B2, B3, and B4) and unilateral ruptures (B1 and B5). Figure 6 shows the rotation invariant measure of SA[1.0 s]). As expected, the highest ground motion intensities are observed in the rupture forward direction. Notably, several of the scenarios present asymmetric ground motion with respect to the faults. Amplified ground motions are located on the respective concave side of the slipping fault. For instance, scenarios B1 and B3 generate stronger ground motions on the northern side of the western segment of the main fault, and on the southern side of the eastern part of the middle segment. Similar to our segmented Model-A based dynamic rupture scenarios, rapid rupture acceleration and deceleration at geometric complexities generate intense ground motions. These fault complexities, e.g. fault bends, pose locally different pre-stress conditions and barriers to rupture propagation. Bands of elevated ground motion form at an acute angle with respect to the rupture direction. This results in asymmetric shaking around the smooth fault (see Figure 6). In addition, smaller scale topography features imprint the ground motion maps as discussed for Model-A scenarios.

#### *3.2.2 "Closed gap" (Model-C)*

Model-B scenarios demonstrate that a significant lateral offset between the Eastern and Central HFFZ can arrest dynamic earthquake rupture and thus reduces the maximum earthquake magnitude possible on the fault system. In this section we "close the gap" (Model-C) to investigate alternative and potentially worst-case-scenarios of dynamic rupture on the HFFZ. We define four dynamic rupture scenarios on the geometry of Model-C by varying hypothetical hypocentral positions (Figure 1b). We use the same model parameters as for Model-B scenarios. For the sake of consistent notation and brevity, we do not show scenario C2 since it is the same as scenario B2.

In contrast to Model-B scenarios, all Model-C scenarios result in rupture of the entire main fault and no activation of other fault branches. This leads to $M_{\mathrm{w}}$7.3 moment magnitudes. The full connectivity of the main fault results in simple rupture dynamics in all scenarios, leading to relatively smooth and homogeneous fault slip distributions that are modulated by the varying hypocenter locations (Figure 7a). As an example, we detail the rupture dynamics of Model-C3 in Figure S2 and Movie S3. Patches of large slip coincide with fault segments relatively far away from the hypocenter. For example, in scenarios C1 and C3, peak slip occurs on the eastern segment, while it localizes on the western segment in scenarios C4 and C5. The smooth fault geometry and lack of small-scale structural heterogeneity in our models promotes a nearly constant rupture speed (Figure 7a). However, the incipient westward rupture in scenario C4 features a few seconds of rupture delay coinciding with the change in fault geometry at the connection between the eastern and middle segments, i.e., where the gap has been closed. The homogeneous rupture speed and slip distribution in all scenarios are manifested in their simple moment rate functions (Figure 7b). Their shapes are modulated by the varying hypocentral locations, which promote either unilateral or bilateral ruptures. Bilateral ruptures are of shorter duration and therefore show higher rate of moment releases.

Maps of ground motions are shown in Figure 8. To better illustrate effects of the rupture directivity and fault geometry, we show the ground motion amplitude distribution along two cross-sections perpendicular to the western (A-A') and eastern (B-B') segments, respectively for two scenarios, C1 and C4. Rupture directivity causes heterogeneous ground motion intensities. Ground motions are amplified in rupture forward direction, illustrated as higher ground shaking amplitudes along cross-section A-A' in scenario C4 than those in scenario C1, and inversely for cross-section B-B'. Depending on the scenario, both symmetric and asymmetric ground motion patterns are observed across a linear fault segments. Ground motion asymmetry is caused by the coupled effect of rupture directivity and fault geometry. For example, the unilateral rupture from west to east in scenario C1 results in a symmetric pattern along the A-A' across the straight fault

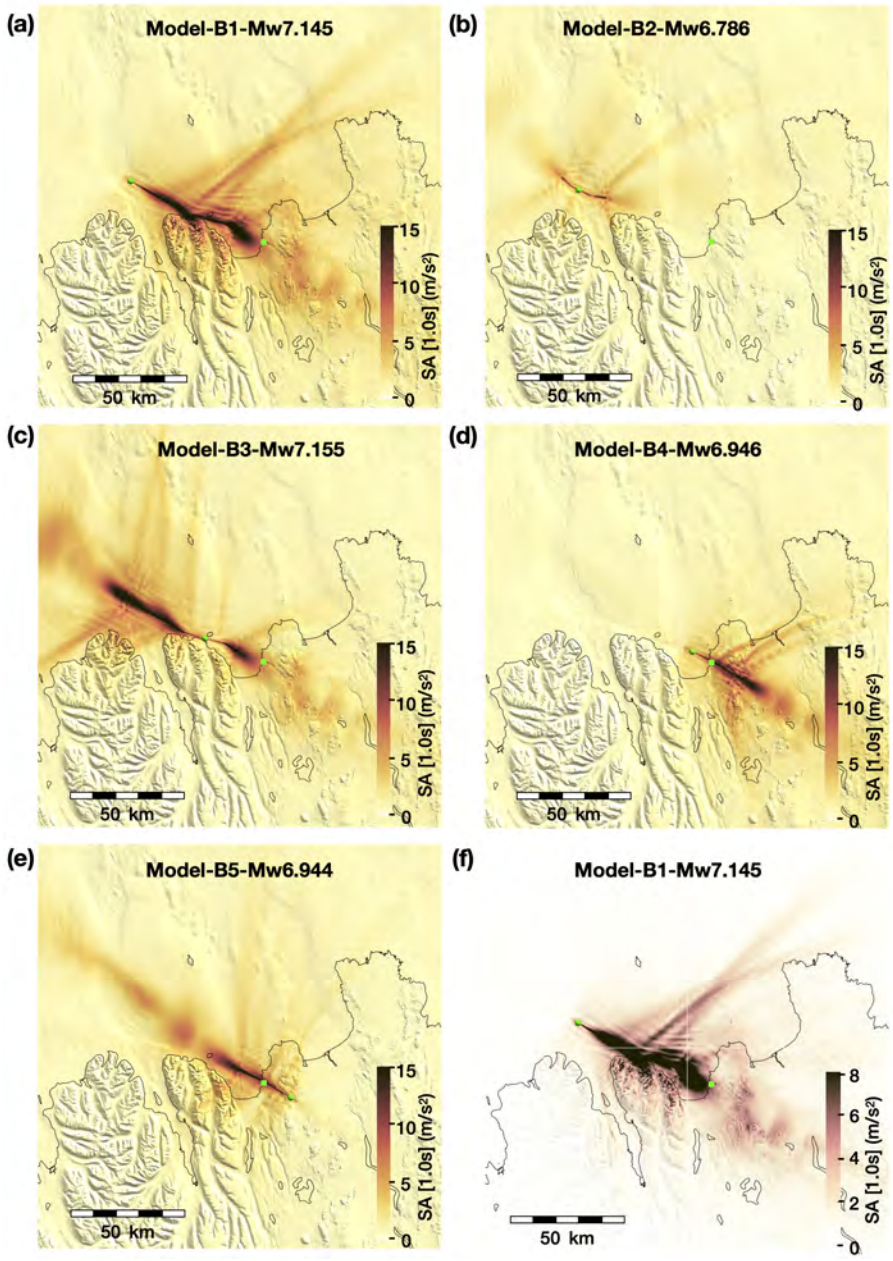


**Figure 6.** Ground motions (spectral acceleration SA[1.0 s] in $m/s^2$) for five rupture scenarios across Model-B, shown in panels (a)-(e). The green circle marks the hypocenter location for each scenario. Color maps are saturated to better capture the spread of the ground shaking away from the fault network. Panel (f) is the same as panel (a), but with a narrower range colormap and using an opacity filter to highlight smaller-scale amplification of topography features.

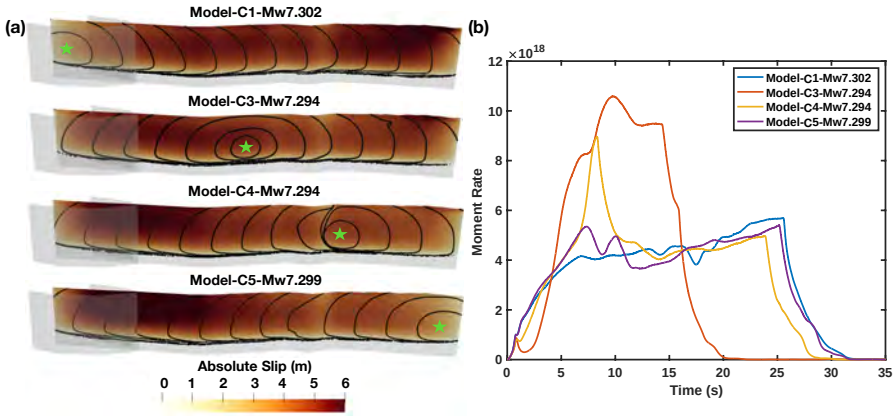


**Figure 7.** All Model-C scenarios rupture the entire main fault and do not activate other fault segments. (a) Accumulated fault slip distribution of four rupture scenarios across Model-C. We omit scenario C2 since it is equivalent to scenario B2. The green stars show the hypocenter locations of each scenario. The black contours are 2 s isochrones of the rupture time. (b) Moment rate functions for the four rupture scenarios in (a).

segment in the west (Figure 8e). In contrast, rupture from east to west in scenario C4 breaks through the fault kink, between the middle and western segments, before reaching the western linear fault segments. This results in an asymmetric pattern along the same cross-section with higher ground motions on the northern side of the fault. The same coupled effect also leads to a symmetric pattern along B-B' across the eastern fault segments for scenario C4 and asymmetric distribution for C1, depending on whether the rupture has broken through fault complexities or not before reaching the linear fault segments.

### 3.3 Fault roughness

Natural faults comprise both large-scale geometrical complexities (e.g., segmentation, branching), but also small-scale roughness (e.g., Power & Tullis, 1991; Ben-Zion & Sammis, 2003; Sagy et al., 2007; Candela et al., 2009; Bistacchi et al., 2011). Fault roughness results in small-scale complexities in pre-stress distribution and poses additional resistance (the roughness drag, Dunham et al. (2011)) to rupture. Fault roughness affects rupture dynamics, ground motion and surface displacements (Dieterich & Smith, 2009; Fang & Dunham, 2013; Bruhat et al., 2020). Rough fault dynamic rupture simulations are able to generate broadband synthetic waveforms comparable with natural earthquakes (Shi & Day, 2013; Withers et al., 2019; Taufiqurrahman et al., 2022). Here we explore the effect of fault roughness based on Model-C. We construct rough faults with a self-similar fractal distribution over length scales from 200 m to 50 km, and assume an amplitude to wavelength ratio $\alpha$ equal to $10^{-2}$, following Shi & Day (2013).

Our simulations incorporating fault roughness leave all other dynamic parameters the same. We show that fault roughness can significantly affect the spatio-temporal evolution of the simulated ruptures and modulate their macro-scale characteristics (e.g., the average fault slip). To identify our 4 scenarios incorporating fault roughness, we append a "-R" to their names. Scenarios C1-R and C5-R have slightly lower magnitudes than scenarios C1 and C5, and their final fault slip distribution is more heterogeneous (Figure 9). Rupture dynamics are affected by fault roughness, especially at the edges of the

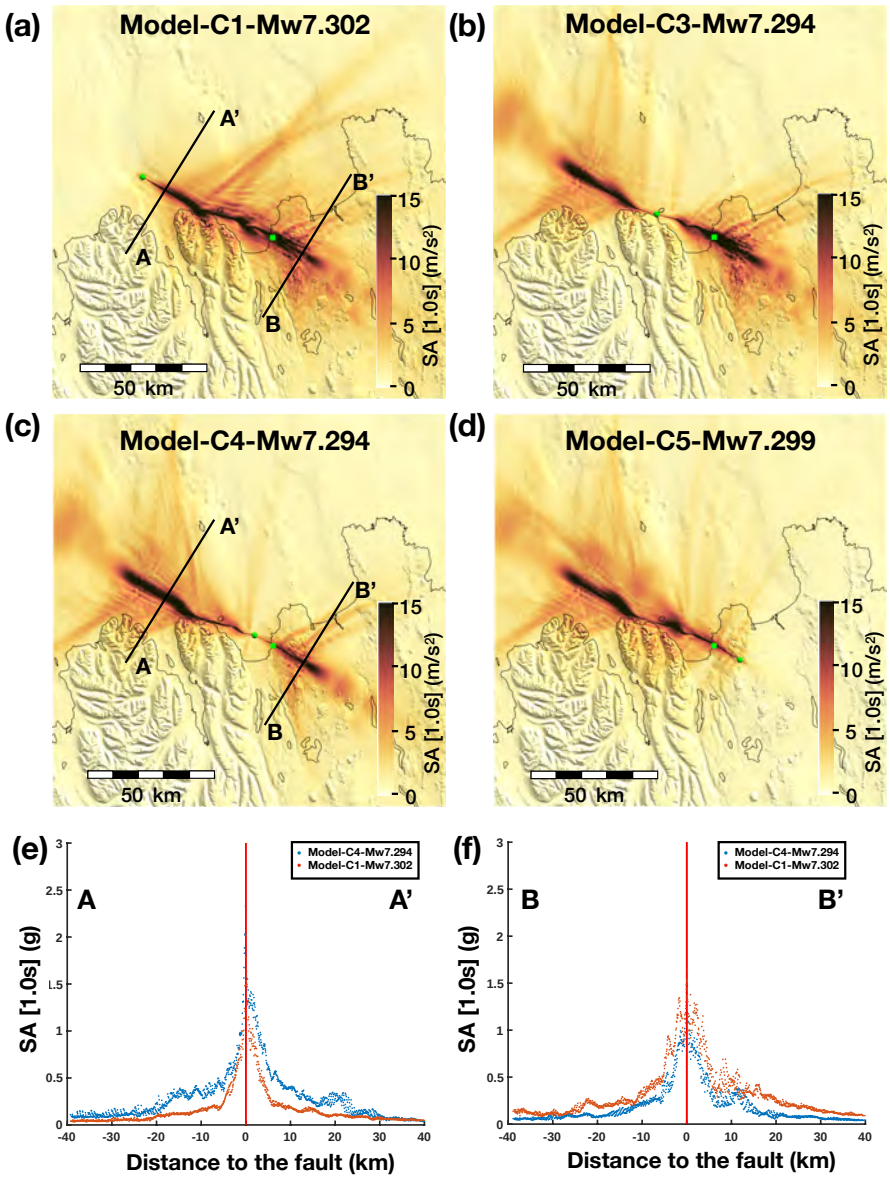


**Figure 8.** (a)-(d) Ground motions (spectral acceleration SA[1.0 s] in m/s$^2$) for four rupture scenarios across Model-C. The green circle marks the hypocenter location for each scenario. The green square shows the location of the Húsavík town that sits on the east segment of the fault. Color maps are saturated to better capture the spread of ground motions. (e)-(f) Ground motions (SA[1.0 s]) along cross sections A-A' and B-B' for scenarios C1 and C4. The vertical red lines show the fault location.

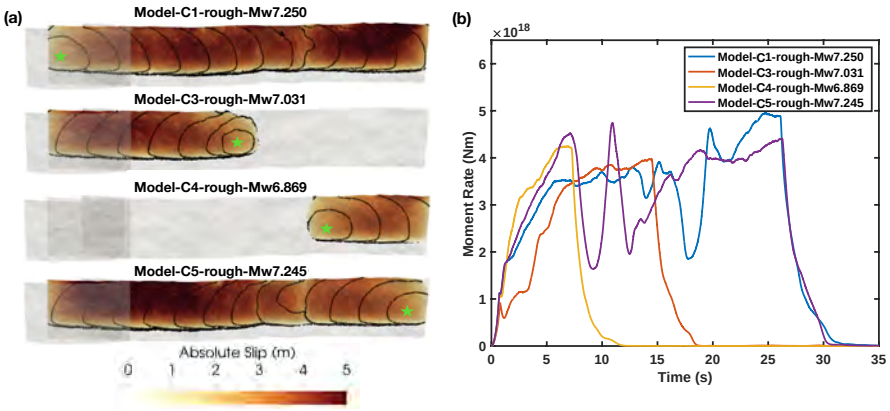


**Figure 9.** (a) Accumulated fault slip distribution of four Model-C scenarios incorporating fault roughness. The green stars show the hypocenter locations of each scenario. The black contours are 2 s isochrones of rupture time. (b) Moment rate functions for the four rupture scenarios in (a)

bend at the location of the closed gap between the central and western sections of the HFFZ. In scenarios incorporating fault roughness, rupture is delayed significantly (scenarios C1-R and C5-R) or partially (scenarios C5-R). It can also be totally arrested (scenarios C3-R and C4-R) at these locations, in contrast to the reference ruptures without fault roughness. Delayed rupture is associated with a noticable local drop in the moment rate release. We highlight that if fault roughness is incorporated, scenarios based on Model-C (scenarios C3-R and C4-R) can reproduce historic magnitude 7 earthquakes which was not the case without fault roughness. Fault roughness allows physics-based generation of high frequencies. We observe higher frequencies but lower ground motion amplitudes at moderate frequencies (1 s period), especially in the near field region (Figure S3). Variations in the high frequency radiated spectra are expected and depend on the local rupture velocity and the roughness profile (Dunham et al., 2011).

### 3.4 Sensitivity to model parameter variations

As stated in Section 2.3 our prescribed depth-dependent initial fault stress and relative strength are controlled by four parameters: the orientation of the maximum horizontal compressive stress $SH_{\max}$, the stress shape ratio $s2_{\text{ratio}}$, the pore fluid pressure ratio $\gamma$ and the maximum pre-stress ratio $R_0$. We perform sensitivity analysis by varying these four parameters and investigating how they affect the resulting rupture dynamics on the HFFZ. We use the simplest model of the fault network, Model-C, to isolate each effect.

The trade-offs of these parameters within observational uncertainties are partially constrained by historic earthquake magnitudes, scaling relations and matching empirical ground motion models (see next Section 4). Variations in these four parameters affect the average stress drop in our dynamic models, in turn governing the average fault slip, rupture speed, and earthquake magnitude. For example, a high average stress drop leads to supershear rupture and unrealistically large slip, whereas a low value results in rupture terminating early (Ulrich, Gabriel, et al., 2019). Improved (near-fault) observational and physical constraints may mitigate the dynamic trade-offs due to modeling parameters that we discuss in the following.

Previous studies suggest $SH_{max} = 155 \pm 22°$ clockwise from north (Ziegler et al., 2016; Angelier et al., 2004). Thus, we here vary $SH_{max}$ in the range from 135 to 170°, in steps of 5° with all other parameters remaining unchanged. We conduct the sensitivity analysis for three hypocenter locations, on the east (Figure 10a), middle (Figure 10b) and west (Figure 10c) segment of the main fault, respectively. Because of differences in fault orientation along the main fault, rupture extent and fault slip distribution vary with both hypocenter position and $SH_{max}$ orientation (Figure 10). Full main fault rupture is achieved for $SH_{max}$ of 140° to 155° for hypocenters in the eastern or middle segments. $SH_{max}$ needs to be between 150° and 160° for full main fault rupture when the hypocenter is chosen on the western segment. Partial rupture of one or two segments of the main fault is also possible for specific combinations of hypocenter location and $SH_{max}$. We note that analogous to static slip tendency analysis (e.g., Morris et al., 1996), we can perform a "dynamic" slip tendency analysis without running dynamic rupture simulations. Analysis of the fault-local distributions of initial relative fault strength $R \leq R_0$ and the ratios of initial shear and normal stresses reveal more favourable dynamic parameters for sustained rupture scenarios (as in Ulrich, Vater, et al., 2019; Palgunadi et al., 2020). However, complex rupture dynamics, such as dynamic triggering, are only accessible from dynamic rupture simulations.

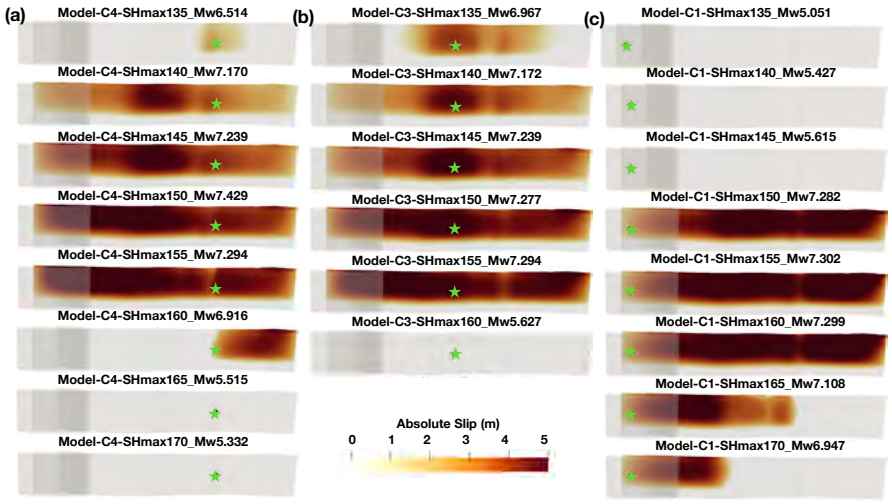


**Figure 10.** Sensitivity of dynamic rupture scenarios using Model-C under $SH_{max}$ variations in the range from 135° to 170°. We show the accumulated fault slip (in [m]) for three hypocenter locations, on the east (a), middle (b) and west (c) segments, respectively. The moment magnitude of each scenario is indicated in the title of each figure.

Next we vary the the stress shape ratio $s2_{ratio}$ between 0.4 and 0.9, with all other parameters remaining unchanged. Figure 11 shows dynamic rupture scenarios for three hypocenter locations, in the east, middle and west segments. A $s2_{ratio}$ different from 0.5 (pure strike-slip) may favor more complex multi-fault ruptures, by loading both strike-slip and ∼60 degree dipping normal or ∼30 degree dipping thrust faults, depending on $s2_{ratio}$>0.5 or <0.5. However, our fault models assumes vertically dipping segments, see Section 2.1. The $s2_{ratio}$ also adjusts the magnitude of the horizontal principal stress relative to the vertical principle stress, which is $s2$ in our model. Thus, a smaller $s2_{ratio}$ leads

to larger $s_1 - s_3$ which results in larger fault slip and earthquake magnitude. In addition, rupture nucleated on the east or west segments are able to break the less optimally oriented middle segment when $s2_{\text{ratio}} > 0.5$.

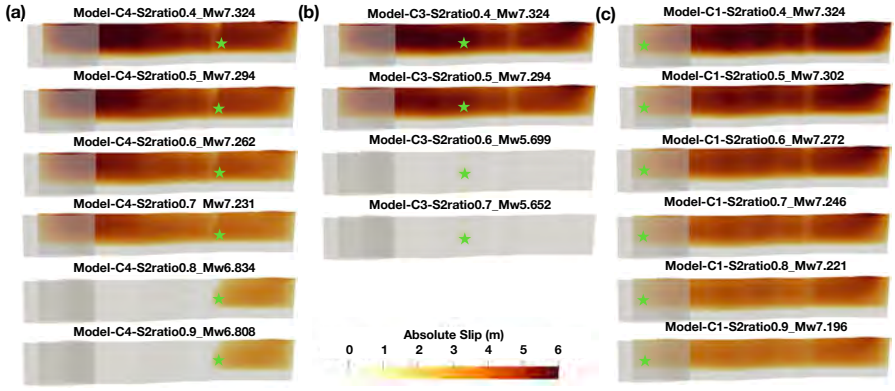


**Figure 11.** Sensitivity of dynamic rupture scenarios across Model-C to $s2_{\text{ratio}}$ variations in the range from 0.4 to 0.9 for three hypocenter locations, in the east (a), middle (b) and west (c) segments, respectively, with illustration of the accumulated fault slip distribution (in [m]). The moment magnitude of each scenario is indicated in the title of each figure.

Figure 12 shows the effect of the pore fluid pressure ratio $\gamma$ modulating the confining stress gradient (Madden et al., 2022), and therefore the potentially available stress drop. Lower $\gamma$ are associated with larger earthquake magnitudes, and higher peak slip. A higher $\gamma$ is associated with a lower effective normal stress, and therefore requires larger critical nucleation size for self-sustained dynamic rupture. This explains why higher $\gamma$ scenarios are associated with partial rupture or failed nucleations. We observe differences with varying hypocenter locations, which stem from the different orientations of each segment relative to the regional stress optimal orientation.

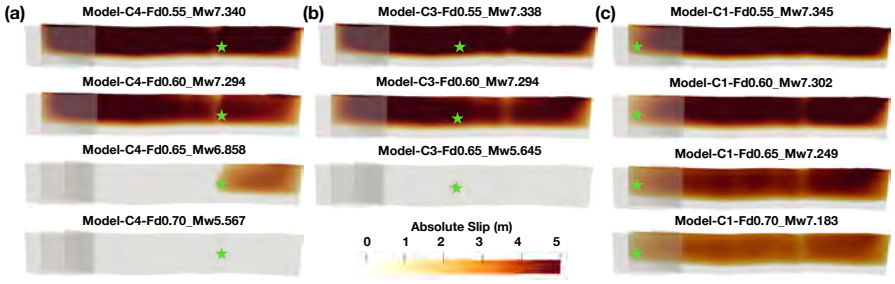


**Figure 12.** Sensitivity of dynamic rupture scenarios across Model-C to $\gamma$ variations in the range from 0.55 to 0.7 for three hypocenter locations, in the east (a), middle (b) and west (c) segments, respectively, with illustration of the accumulated fault slip distribution (in [m]). The moment magnitude of each scenario is indicated in the title of each figure.

We lastly vary the maximum pre-stress ratio $R_0$ in the range from 0.45 to 0.65, with all other parameters remaining unchanged. Figure 13 shows these dynamic rupture scenarios for three hypocenter locations, in the east, middle and west segments. The relative pre-stress ratio $R$ is related to the classical seismic S-ratio (Andrews, 1976) as $R = 1/(S+1)$. The local fault orientation controls the pre-stress at any point on the fault, with always $R \leq R_0$. Locally higher $R$ corresponds to a greater tendency for dynamic rupture (e.g., Biemiller et al., 2022). For $R = R_0$, the fault segment is optimally oriented with respect to the local stress conditions. When $R_0$ approaches 1, all optimally oriented fault segments approach critical pre-stress levels. Full rupture is achieved for $R_0 \geq 0.55$ for earthquake nucleation in the eastern or middle segment, and $\geq 0.50$ when the hypocenter is on the western segment. We note that spontaneous partial rupture of one or two segments can be modeled for each hypocenter location by specific choices of $R_0$, not shown here but illustrated by the partial rupture of the eastern segment when choosing $R_0$ =0.5 and the hypocenter to the east.

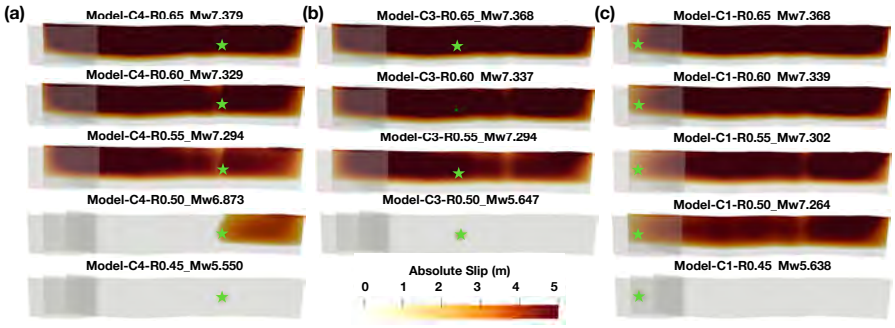


**Figure 13.** Sensitivity of dynamic rupture scenarios using Model-C geometry under $R_0$ variations in the range from 0.45 to 0.65 for three hypocenter locations, in the east (a), middle (b) and west (c) segments, respectively, with illustration of the accumulated fault slip distribution (m). The moment magnitude of each scenario is indicated in the title of each figure.

## 4 Synthetic ground motion characteristics

The ground motion synthetics resulting from all physics-based earthquake scenarios in this study show heterogeneous distributions along and across the fault system. We resolve (dynamic) effects that are not, or not fully, accounted for in empirical ground motion prediction equations (GMPEs) or ground motion models (GMMs). For near-fault motions, our simulated ground shaking intensities are strongly affected by the effects of geometric fault complexity (e.g., fault segmentation or gaps), the dynamic irregularities of the propagating rupture (e.g., local acceleration and deceleration, dynamic triggering, backward-propagating fronts), forward directivity effects and topography amplification.

### 4.1 Forward directivity effects

The constructive interference of long-period seismic waves due to the geometry of the fault and the propagating rupture front leads to forward directivity effects that amplify seismic ground motions as much as one order of magnitude (e.g., P. Somerville & Graves, 1993; P. G. Somerville et al., 1997; Mavroeidis & Papageorgiou, 2003; Pacor et al., 2016). Such directivity effects are the most damaging feature of seismic waves in the

near-fault region and are therefore increasingly being incorporated in near-fault seismic hazard assessment (Kurzon et al., 2014; Graves et al., 2011; Chen et al., 2018, e.g.,). In addition, rupture directivity is able to affect the spectrum of ground motions even in teleseismic distances(e.g., Li et al., 2022). We quantify the variability of directivity effects on synthetic ground shaking, by analyzing the azimuthal dependence of our modeled intensities for various Joyner-Boore distances ($R_{JB}$). $R_{JB}$ is defined as the shortest horizontal distance from a site to the vertical projection of the rupture plane (Abrahamson & Shedlock, 1997). We use bins of 4° for the azimuth, calculated relatively to the epicenter, and the following $R_{JB}$ ranges: 2-5 km, 10-20 km, 30-45 km and 1-45 km. For each bin, we compute the average spectral acceleration at 1.0 s.

Figure 14 shows the azimuthal dependence of SA[1.0 s] for the four Model-C scenarios of Section 3.2.2. Unilateral ruptures (scenarios C1 and C5) result in a unimodal azimuthal distribution with peak ground shaking in the rupture forward direction. Directivity-amplified ground motions occur for azimuths ranging between 100 and 140° for scenario C1 and for azimuths between 275 to 315° for scenario C5. The peaks fall at 118 and 298°, respectively, in opposite directions. Bilateral ruptures (scenarios C3 and C4) lead to bimodal distributions, with two peaks appearing at the same azimuths as in C1 and C5.

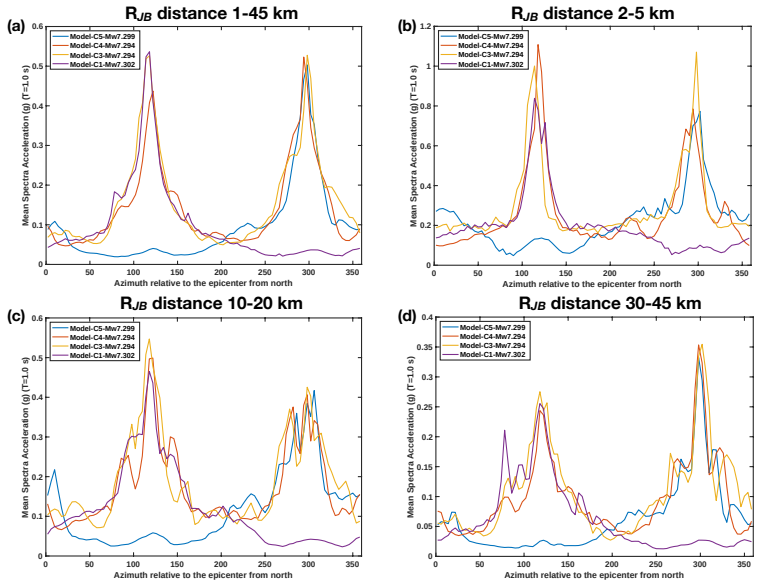


**Figure 14.** Azimuthal dependence of synthetic SA[1.0 s] for the four rupture scenarios based on Model-C (Figure 8), illustrating directivity effects. Results are shown for Joyner-Boore distance ($R_{JB}$) ranges of 1-45 km (a), 2-5 km (b), 10-20 km (c) and 30-45 km (d), respectively.

To quantify how rupture directivity effects vary across Model-C scenarios, we use the Cauchy-Lorentz function. This function can be expressed as:

$$y(x) = \frac{I\kappa^2}{(x - x_0)^2 + \kappa^2} + C.$$

In this equation, $x$ is the azimuth, $y$ is the ground shaking intensity measure, and $I$, $\kappa$ and $C$ are free parameters. While $I$ allows modulating the increase of ground shaking intensity in the forward rupture direction relative to the backward direction, $\kappa$ is the half-width of the peak of the function, and $x_0$ is the location of the peak. $C$ is a constant value that determines the ground shaking intensity baseline. The peak ground motion for scenarios C1 and C5 are aligned with the main fault strike, at azimuths (clockwise to the north) 118° and 298°, respectively. As we expect rupture directivity effects to peak around these azimuths in all simulations, we restrict the range of possible $x_0$ to ± 90 ° around these reference values. We then search for the Cauchy-Lorentz parameters that minimize the residuals relative to our simulation results using least-squares. The optimal parameters and corresponding residual (sum of squares, RSS) are listed in Table 2. We note that bilateral scenarios can be fit by two Cauchy-Lorentz functions. For all scenarios,

| **Models** | **Directivity relative to 118°** | | | | | **Directivity relative to 298°** | | | | |
|---|---|---|---|---|---|---|---|---|---|---|
| | $I$ | $\kappa$ | $x_0$ | $C$ | **RSS** | $I$ | $\kappa$ | $x_0$ | $C$ | **RSS** |
| **C1** | 0.44 | 12.35 | -1.74 | 0.07 | 0.023 | | | | | |
| **C3** | 0.46 | 15.79 | -2.00 | 0.04 | 0.012 | 0.37 | 18.81 | -0.28 | 0.06 | 0.044 |
| **C4** | 0.34 | 13.25 | 2.51 | 0.07 | 0.017 | 0.41 | 17.49 | -3.95 | 0.04 | 0.023 |
| **C5** | | | | | | 0.41 | 12.67 | -1.39 | 0.07 | 0.009 |
| **C1 (2-5 km)** | 0.66 | 11.6 | -0.74 | 0.16 | 0.057 | | | | | |
| **C1 (10-20 km)** | 0.32 | 25.96 | -0.94 | 0.07 | 0.032 | | | | | |
| **C1 (30-45 km)** | 0.19 | 36.81 | -3.19 | 0.01 | 0.034 | | | | | |
| **C3 (2-5 km)** | 0.87 | 8.25 | -5.76 | 0.17 | 0.060 | 0.76 | 8.2 | -1.76 | 0.20 | 0.182 |
| **C3 (10-20 km)** | 0.43 | 16.79 | -0.49 | 0.08 | 0.057 | 0.31 | 35.04 | -1.73 | 0.04 | 0.075 |
| **C3 (30-45 km)** | 0.23 | 23.56 | 1.89 | 0.02 | 0.012 | 0.28 | 10.41 | 3.83 | 0.07 | 0.047 |
| **C4 (2-5 km)** | 0.91 | 8.68 | 0.87 | 0.14 | 0.059 | 0.62 | 13.20 | -6.47 | 0.13 | 0.106 |
| **C4 (10-20 km)** | 0.35 | 13.08 | 3.01 | 0.11 | 0.087 | 0.31 | 24.21 | -4.09 | 0.06 | 0.057 |
| **C4 (30-45 km)** | 0.17 | 15.24 | 3.85 | 0.05 | 0.012 | 0.26 | 15.86 | 1.00 | 0.04 | 0.043 |
| **C5 (2-5 km)** | | | | | | 0.54 | 9.12 | 0.67 | 0.24 | 0.045 |
| **C5 (10-20 km)** | | | | | | 0.26 | 19.53 | -1.06 | 0.11 | 0.060 |
| **C5 (30-45 km)** | | | | | | 0.24 | 10.71 | 1.42 | 0.07 | 0.020 |

**Table 2.** Parameters of the best-fit Cauchy-Lorentz function modeling the azimuth dependence of mean ground shaking (SA[1.0 s]) for Model-C rupture scenarios.

$I$ decreases with distance highlighting the distance-dependent character of our modeled directivity effects. Generally, $\kappa$ conjointly increases, indicating a less narrow azimuth amplification and weaker directivity effect with distance. Notable exceptions include rupture directivity in the azimuth 298° direction, where $\kappa$ is smaller in the distance range 30-45 km, than in the 10-20 km distance range. The locally higher ground motion amplification, also visible in Figures 8, may be due to the lower seismic velocities in the zone northwest of the HFFZ.

Seismic waves radiated from a decelerating rupture at geometric barriers can strongly affect ground motions on a local scale. Because we calculate the azimuth relatively to the epicenter and not the locations of geometric barriers, the imprint of these waves on ground motion in the near fault region appears in the azimuth range corresponding to the rupture direction, and cannot be easily dissociated from rupture directivity effects. Further away from the fault, both effects can be separated. The curve associated with scenario C1 in Figure 14d presents a local peak in the range 70-80°, which corresponds to a narrow phase radiation band to the northeast direction, associated with the fault

bend linking the western and central sections of the HFFZ. The local effect of such "corner phase" radiation (Oglesby & Mai, 2012) can be also noticed in the curve associated with scenario C5 in Figure 14d. There we see two local peaks at around 270 and 320° close to the global peak at ∼300°. The corner phase effect is consistent with isochrone acceleration leading to strong seismic radiation (Bernard & Madariaga, 1984; Spudich & Frazer, 1984).

The curves associated with scenario C5 in Figure 14 show that the ground shaking intensities do not decay smoothly from the rupture forward direction to the backwards direction. The increase in the azimuth range 210°-250° correlates with the elevated topography region south of the HFFZ. The shielding and focusing effects of topography and bathymetry on the ground motion amplitudes are a site-specific feature affecting modeled ground shaking in addition to the geometric effects of the propagating rupture front.

### 4.2 Comparison with new hybrid Bayesian empirical ground motion models

GMMs describe the level of ground motion, given earthquake source properties (magnitude, faulting mechanism), source to site distance, and site response. They are a key element of PSHA (e.g., Field et al., 2003; Nekrasova et al., 2014; Silva et al., 2020). The majority of GMMs are based on observations from the most seismically active areas. These regional attenuation relationship may not be directly applicable to other regions, of which Iceland is a prime example (see Kowsari et al., 2020, and references therein). To cope with this problem, logic tree approaches combining different regional GMMs have been used in regions where attenuation relationships are not well constrained (e.g., Cotton et al., 2006; Bommer & Stafford, 2020). However, this approach is of little use when the underlying GMMs are unable to appropriately capture the salient features of the existing strong-motion data for the region. Recently, Kowsari et al. (2020) calibrated hybrid Bayesian GMMs for Iceland and for all oscillator periods of engineering interest. In the following, they serve as a baseline for the comparison of the ground motion distribution from the physics-based synthetic ground motions in this study with those of actual data.

The synthetic ground motions from Model-B scenarios compare well with the new GMMs that have been calibrated to the available strong-motion dataset for Iceland (Kowsari et al., 2020) for scenarios with $M_{\mathrm{w}}$ greater than 6.9 in both near- and far-field (Figure 15a,c-e), but show lower amplitude ground motions than the GMMs for smaller magnitudes in the near-field (Figure 15b). Rupture scenarios of similar magnitudes and involving the same faults (B1 and B3, B4 and B5), show nearly identical attenuation relationship in the near field, even if the ground motion distribution differs significantly among scenarios. The ground motion synthetics of the four scenarios based on model-C also compare well with GMMs (Figure 16), and yield very similar average attenuation relationships, especially in the near-field region up to 20 km $R_{JB}$ distance, despite the different ground shaking patterns they produce.

The logarithmic standard deviation $\sigma$ (e.g., Strasser et al., 2009) of GMMs quantifyies ground motion variability (Atik et al., 2010). It may strongly impact seismic hazard assessment. $\sigma$ aggregates many sources of aleatory and epistemic uncertainty, and is often considered to be a constant value in GMMs. Figure 17 shows the distance dependence of $\sigma$ of the SA[1.0s] for the aforementioned five scenarios across Model-B (left) and four scenarios across Model-C (right). For both models, the obtained $\sigma$ is on average higher than the constant intra-event variability (0.573) from Boore & Atkinson (2008) within 50 km $R_{JB}$ distance. $\sigma$ is higher in the unilateral rupture scenarios (e.g., scenarios B1, B5, C1, and C5, with $\sigma$ in 0.6-0.9), than that in the bilateral rupture scenarios (scenarios B2, B3, B4, C3, and C4, with $\sigma$ in 0.5-0.7).

We list in Table 3 the simulated ground shaking (SA[1.0 s]) at seven towns for earthquake scenarios based on all three geometry models. Húsavík, the second largest town

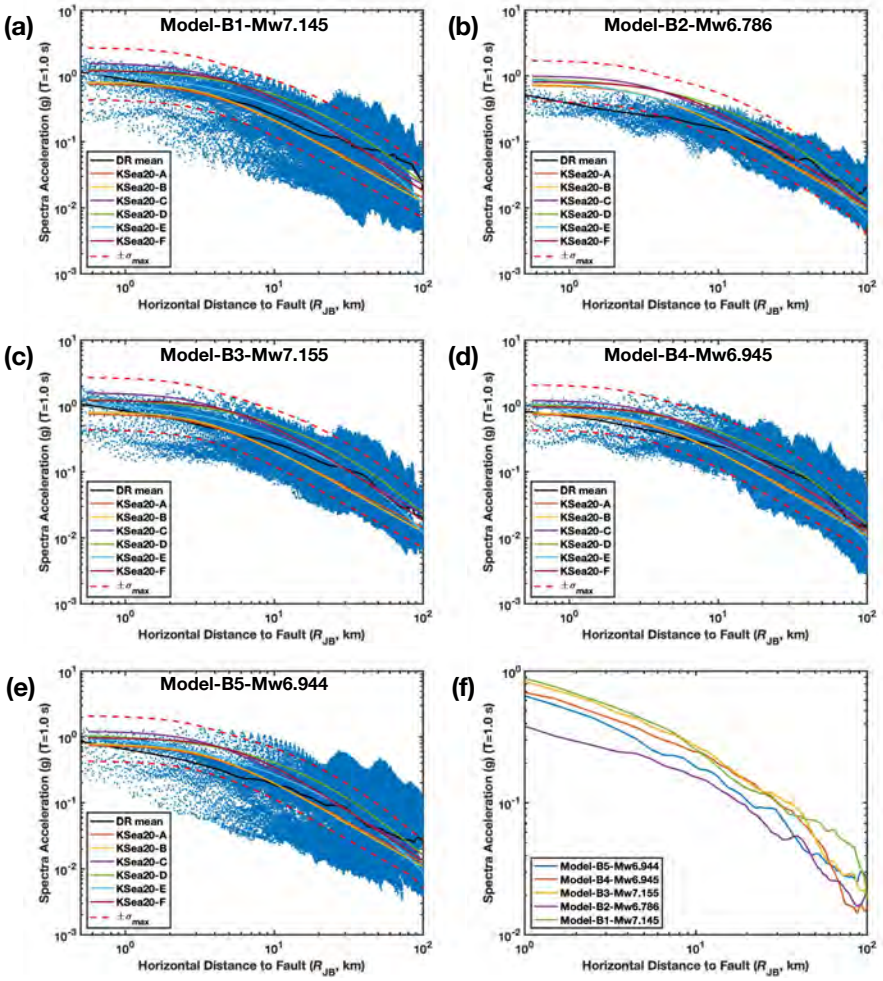


**Figure 15.** Comparison of the synthetic ground motion from earthquake scenarios across Model-B and ground motion models (GMMs), in terms of spectral acceleration (SA[1.0 s], in $m/s^2$) are presented in panels from (a)-(e). The synthetic ground motion at each cell of the triangulated ground surface output is shown with scattered blue dots. The synthetic average attenuation relationship is shown by the black line. Colored solid lines show the mean value of each GMM, for the same moment magnitude as simulated. The dashed lines indicate the largest standard deviation value of all considered GMMs. (f) Mean attenuation relationship for the five rupture scenarios across Model-B.

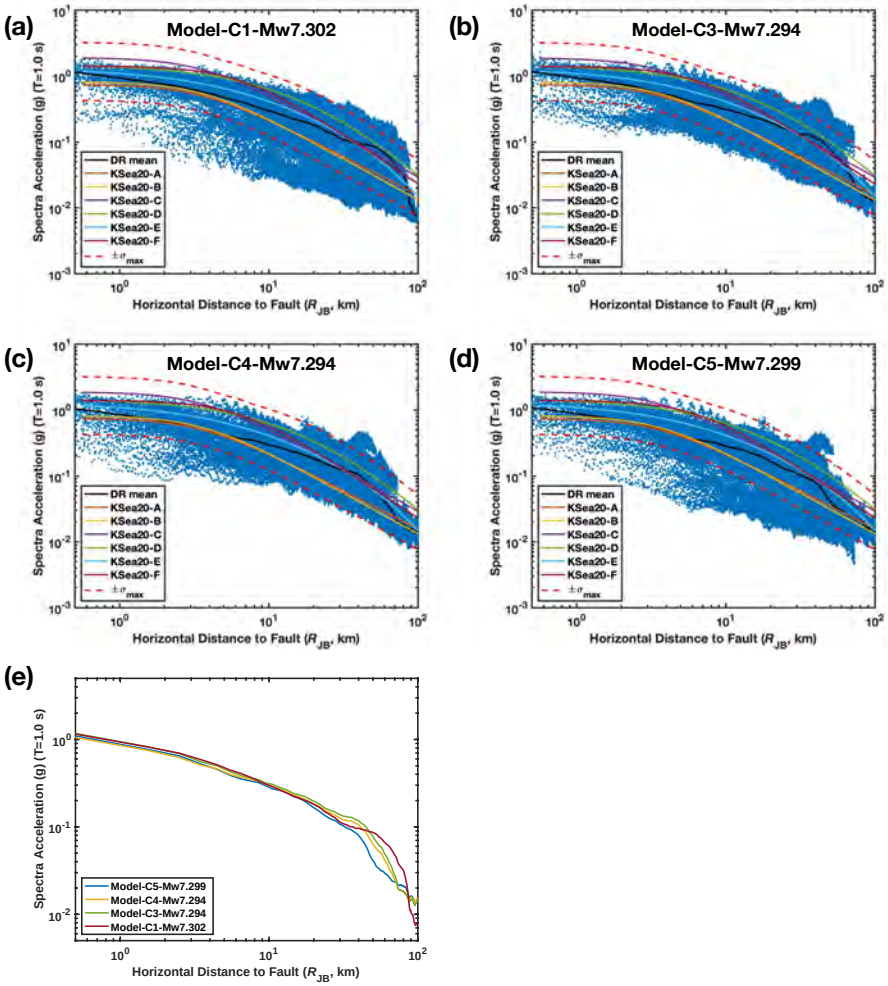


**Figure 16.** (a)-(e) Comparison of the synthetic ground motion from earthquake scenarios across Model-C and ground motion models (GMMs), in terms of spectral acceleration (SA[1.0 s], in m/s$^2$). see caption of Figure 15 for more details. (e) Mean attenuation relationship for the four rupture scenarios across Model-C.

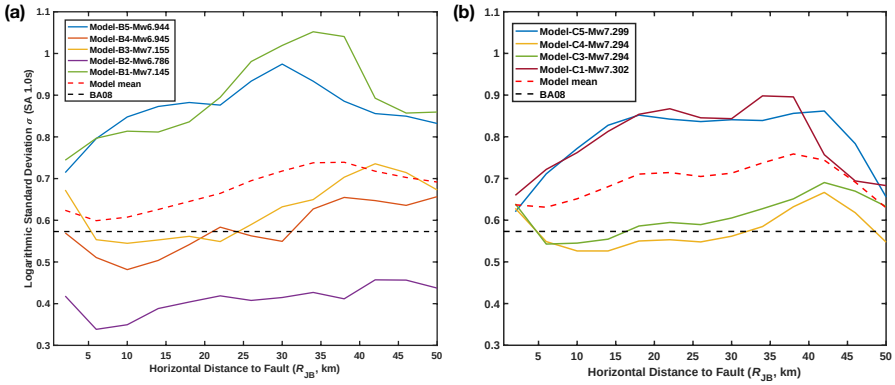


**Figure 17.** Variation with source $R_{JB}$ distance of the (logarithmic) standard deviation of the ground motion synthetics (spectral acceleration SA[1.0 s] in m/s$^2$) for Model-B (Left) and Model-C (Right) compared with Boore & Atkinson (2008). The standard deviation of each scenario (intra-event standard deviation) is plotted with solid lines of different colors. The red dashed line shows the mean standard deviation, and the black dashed line is the constant standard deviation (0.573) inferred by Boore & Atkinson (2008).

in this area, is located on the eastern segment of the HFFZ and experiences in most scenarios the strongest ground shaking. Among all simulated scenarios, the strongest ground motion at Húsavík town is SA[1.0s]=∼1.55 g for the $M_{\rm w}$7.3 scenario C3. Scenario C3 is nucleated in the central section of the HFFZ, and breaks the whole main fault. At Húsavík, $M_{\rm w}$7.3 scenarios C4 and C5 and $M_{\rm w}$6.9 scenarios B4 and B5 generate similar levels of ground shaking, despite their differing earthquake magnitudes. This suggests that for such large earthquakes, a small portion of the ruptured faults can locally dominate near field ground shaking. Scenario A2, of similar magnitude as scenarios B4 and B5, generates weaker ground shaking in Húsavík, possibly due to smaller peak slip rates on the eastern section of the HFFZ, combined with weaker directivity effects associated with shorter fault segments(Wang & Day, 2020). However, scenarios based on Model-A result in stronger ground shaking than Model-B and Model-C in other towns further away from the fault system, especially in Dalvík, Ólafsfjörður and Grenivík. This effect is due to the less attenuated seismic radiation from multiple geometric complexities. The ground shaking of scenarios with roughness (scenarios C1-R and C5-R) at Húsavík is weaker than in the reference scenarios without roughness (scenarios C1 and C5), by about a factor 2 for scenario C1. This may be the consequence of less coherent signals from small and localized radiation (Graves & Pitarka, 2016).

## 5 Discussion

### 5.1 Effect of geometry, hypocenter location and initial stress on fault system rupture dynamics

Our dynamic rupture simulations demonstrate that the fault system geometry, hypocenter location, and initial stress conditions strongly affect earthquake rupture dynamics, slip amplitude and distribution, and the moment magnitude of the fully dynamic scenarios in the HFFZ. The level of complexity of the assumed fault model is a key parameter constraining the final magnitude of our earthquake scenarios, their rupture duration, and dynamic complexity.

| MODEL | Mw | Húsavík | Akureyri | Dalvík | Ólafsf. | Sigluf. | Grenivík |
|---|---|---|---|---|---|---|---|
| **A1** | 6.76 | 0.06 | 0.05 | 0.08 | 0.11 | 0.17 | 0.10 |
| **A2** | 6.91 | 0.36 | 0.08 | 0.15 | 0.13 | 0.06 | 0.21 |
| **A3** | 6.50 | 0.32 | 0.04 | 0.05 | 0.03 | 0.02 | 0.06 |
| **B1** | 7.145 | 0.60 | 0.04 | 0.05 | 0.04 | 0.04 | 0.08 |
| **B2** | 6.786 | 0.03 | 0.01 | 0.03 | 0.03 | 0.07 | 0.03 |
| **B3** | 7.155 | 0.52 | 0.02 | 0.03 | 0.07 | 0.14 | 0.04 |
| **B4** | 6.945 | 0.66 | 0.02 | 0.02 | 0.02 | 0.01 | 0.04 |
| **B5** | 6.944 | 0.79 | 0.02 | 0.04 | 0.03 | 0.03 | 0.05 |
| **C1** | 7.302 | 1.41 | 0.06 | 0.08 | 0.05 | 0.07 | 0.09 |
| **C1-R** | 7.250 | 0.79 | 0.05 | 0.09 | 0.05 | 0.05 | 0.09 |
| **C3** | 7.294 | 1.55 | 0.02 | 0.06 | 0.09 | 0.20 | 0.03 |
| **C3-R** | 7.031 | 0.03 | 0.01 | 0.03 | 0.05 | 0.15 | 0.02 |
| **C4** | 7.294 | 0.63 | 0.02 | 0.08 | 0.09 | 0.22 | 0.05 |
| **C4-R** | 6.869 | 0.46 | 0.02 | 0.01 | 0.01 | 0.01 | 0.01 |
| **C5** | 7.299 | 0.80 | 0.04 | 0.10 | 0.10 | 0.21 | 0.06 |
| **C5-R** | 7.245 | 0.72 | 0.05 | 0.08 | 0.09 | 0.21 | 0.08 |

**Table 3.** Simulated ground motions (SA[1.0 s], g) at selected towns in Northern Iceland for chosen dynamic rupture earthquake scenarios.

Scenarios using the complex Model-A, with its 55 fault segments separated by a variety of gaps and step overs, rupture a significant portion of the whole HFFZ. However, the high segmentation of Model-A does not favor rupture scenarios that result in earthquakes larger than $M_{\rm w}7$. The Model-A dynamic parameters required for sustained earthquake scenarios of realistic magnitude (Table 1), promote direct branching and dynamic triggering (rupture jumping), and, therefore, multi-fault earthquake rupture. We observe forward and backward propagating ruptures of adjacent segments, and episodes of localized supershear rupture velocity (Figure 2). In Model-A scenarios, fault slip distributions are highly heterogeneous. Similar dynamic complexities have been inferred in data-constrained multi-fault dynamic rupture models of well-recorded events, such as the 1992 multi-segment strike-slip Landers, California, earthquake (Wollherr et al., 2019).

In contrast, the less segmented fault systems of Model-B and Model-C are dynamically able to generate $M_{\rm w}7+$ rupture scenarios. The prominent $\sim 4$ $km$ wide compressional step over between the east and middle sections of the HFFZ incorporated in Model-B represents a strong dynamic barrier, effectively limiting rupture propagation of all our Model-B earthquake scenarios and their magnitudes to $M_{\rm w}6.9$-$7.1$. This is not unexpected: field observations and numerical studies suggest that strike-slip earthquake rupture rarely jumps across step overs wider than a few kilometers, especially for compressional step overs (Wesnousky, 1988; Oglesby, 2005; Elliott et al., 2009). Closing the geometric gap in model-C scenarios leads to through-going rupture breaking the complete main fault, resulting in $M_{\rm w} \sim 7.3$ rupture scenarios.

None of our scenarios based on Model-B and Model-C show dynamic triggering between the main fault and the secondary faults of the western HFFZ. The dynamic stress ahead of a westwards propagating rupture front across the right lateral main fault clamps the southern fault, and unclamps the northern fault. The northern fault is not activated in any of our scenarios, due to a $\sim$2 km wide gap separating it from the main fault. The southern fault segments is unclamped when rupture nucleates on the west segment and propagates to the east. But the obtuse angle the southern fault forms with the eastward rupture propagation does not favor dynamic triggering. The dynamic stresses generated by an eastwards propagating rupture of the main fault results in left-lateral shear stress-

ing of the Southern fault (e.g., Poliakov et al., 2002) in contrast to the right-lateral initial shear stress loading this segment due to the regional stress field.

Fliss et al. (2005) propose a mechanism for "backwards branching" of secondary faults that form an obtuse angle with the direction of 2D mode II rupture propagation. They suggest that intense stress radiation from rupture arrest on the main fault can dynamically trigger a neighboring secondary fault in such specific configurations, which can then bilaterally rupture. In Model-B and Model-C, the unsegmented main fault geometry does not offer strong barriers aiding backward triggering of secondary faults of the western HFFZ. We do observe backward branching using Model-A, for instance in scenario A2. Spontaneous rupture arrest on the eastern edge of segment F30 allows rupture jumping to segment F33. New rupture dynamically initiates centrally on F33, which is close to the eastern edge of F30, and propagates bilaterally (Figure 2a) in agreement with earlier 2D analysis (Fliss et al., 2005).

Varying hypocenter locations can affect the final slip distribution and magnitude, as well as the spatio-temporal evolution of earthquake rupture, but the strength of this effect depends on fault geometry. In all scenarios based on the complex geometry of Model-A, only a few fault segments in the hypocentral region rupture. Scenarios of magnitude $M_{\mathrm{w}}6.76$, $M_{\mathrm{w}}6.91$, and $M_{\mathrm{w}}6.50$ are obtained for hypocenters in the west, middle, and east of the HFFZ, respectively (Figure 3). The variation of hypocenter location on the well-connected faults of Model-B has only a minor effect on the final magnitude: $M_{\mathrm{w}}7.145$ and $M_{\mathrm{w}}7.155$ for scenarios B1 and B3, $M_{\mathrm{w}}6.945$ and $M_{\mathrm{w}}6.944$ for scenarios B4 and B5. The slip distributions are significantly modulated by hypocenter location, with larger slip at greater distances from the hypocenter.

Scenarios with different hypocenters differ in their kinematic properties. For instance, scenario B3 has slower rupture propagation in the central segment than scenario B1 (Figure 5). The effect of the hypocenter location on the spatial-temporal evolution of the earthquake rupture is also noticeable in Model-C scenarios. Rupture transition from the eastern to the central section of the HFFZ is delayed in scenario C4, which is nucleated at the main fault bend near the now closed gap, on the eastern section of the HFFZ (Figure 7). When the hypocenter is far from the fault bend, rupture can propagate smoothly across it. Similar hypocenter location effects have been observed in previous finite-source models and dynamic studies for different fault networks (e.g., P. M. Mai et al., 2005; Oglesby & Mai, 2012; Kyriakopoulos et al., 2019).

The smooth main fault bend in Model-C scenarios does allow some ruptures to propagate across while terminating others depending on the local pre-stress and dynamic stress evolution. The bend acts as a so-called "earthquake gate" (e.g., Liu et al., 2021, 2022). The segmented, explicitly modeled geometrical barrier posed by the open gap in our Model-B scenarios, however, is different and can effectively stop all dynamically plausible rupture scenarios. This highlights the importance to acknowledge segmented fault system geometries when studying earthquake gates such as the Big Bend or the Cajon Pass of the Southern San Andreas fault and Nothern San Jacinto fault (Lozos, 2016), respectively.

The effect of fault geometry and hypocenter location on earthquake rupture evolution and magnitude of rupture scenarios is dependent on the initial stress conditions (see Section 3.4). Our sensitivity analysis of the pre-stress related initial parameters– $SH_{\mathrm{max}}$, $s2_{\mathrm{ratio}}$, $\gamma$ and $R_0$, show that rupture transitions between multiple segments of the main fault are differently affected by fault geometry and hypocenter location depending on the initial dynamic parameters (Figure 10, 11 12, 13). The non-linearity relating initial conditions to fault geometry, render 3D complex dynamic rupture simulations as an indispensable tool for fully physics-based earthquake scenarios and ground motion modeling.

### 5.2 Limitations and future work

Future extensions of our study may address the challenges in observationally constraining our earthquake scenarios. Specifically, the variability of the locking depth, the connection or disconnection between fault segments and the 3D variability of fault stress and strength are poorly constrained. We here assume in all models a purely strike-slip loading ($s2_{\text{ratio}}$=0.5) and depth-dependent background stress and fault strength parameters and omit potential additional along-strike heterogeneity. However, our effective fault pre-stress is 3D heterogeneous due to the modulation by fault geometry.

Due to the offshore location of the mostly submerged fault system and limited data coverage, the locking depth of HFFZ is poorly constrained. Seismotectonic analysis of Rögnvaldsson et al. (1998) suggests a locking depth of 10 km-12 km in the TFZ, while GPS analyses indicates a shallower locking depth of 5 km (Árnadóttir et al., 2009) or $6.3^{+1.7}_{-1.2}$ km (Metzger et al., 2011), or 6 km-10 km using combined GPS and InSAR data (Metzger & Jónsson, 2014). The lower thermal gradients in the west of the HFFZ may be associated with local variations of the locking depth. The seismogenic depth could decrease from west to east (Flóvenz & Saemundsson, 1993; Metzger et al., 2011). Here, we smoothly taper deviatoric stresses below 9 km depth over 2 km, without lateral variations. Future models may study the effects of a variation of locking depth on rupture dynamics, slip amplitude, earthquake magnitude and ground shaking (e.g., Smith-Konter & Sandwell, 2009; Kyriakopoulos et al., 2019; Oglesby, 2020). However, we expect that our main conclusions on the relative effects of fault geometry, hypocenter locations (rupture directivity) and topography on rupture dynamics and ground shaking in the HFFZ will remain valid with a different locking depth.

We model the HFFZ with both a complex fault geometry (Model-A) consisting of 55 fault segments and two more simple fault geometries (Model-B and Model-C) consisting of 4 or 3 faults. It is possible that the actual fault system geometry falls in between, or shows discontinuities at the surface but a highly connected geometry at depth, as it has been suggested for other mature fault networks (e.g., Elliott et al., 2009), motivating further analysis of fault geometry effects. Our assumed regional, depth-dependent pre-stress results in similar stress conditions for similarly oriented fault segments. However, Passarelli et al. (2018) infer normal faulting focal mechanisms in the western HFFZ. Heterogeneous fault stresses unrelated to fault geometry may build up throughout the long-term seismic cycle, specifically in fault systems featuring stark geometric complexities and step-overs (Duan & Oglesby, 2006). These effects may be captured in future combination of dynamic rupture scenarios with seismic cycle simulations (e.g. Galvez et al., 2020).

Our dynamic rupture simulations can complement GMM-based approaches for assessing the seismic hazard in the HFFZ. Our synthetic ground motions agree well with specific GMMs developed in the tectonically and seismically symmetric SISZ (Kowsari et al., 2020), in terms of their average attenuation relationships (Figures 15 and 16). In addition, the average ground motions show magnitude-consistent attenuation relationships in our synthetic scenarios when breaking the same fault segments. This makes it possible to derive a physics-based GMM from dynamic rupture simulations. Also, our dynamic rupture scenarios can match the inferred characteristics of historical events, such as moment magnitude and rupture extent (Section 3.1). The here developed physics-based approach may be applied to other regions with limited seismic databases. An important advantage of dynamic rupture scenario based ground motion modeling is the physically realistic source description. The synthetic ground motion accounts realistically and self-consistently for complex path effects within 3D velocity structure, source directivity, and local site conditions (basin effects, topography and bathymetry). Fully considering shallow site effects may further amplify high-frequency content of our synthetics (e.g. Rodgers et al., 2020).

## 6 Conclusion

We present physics-based earthquake scenarios across the Húsavík–Flatey fault zone (HFFZ) based on 3D spontaneous dynamic rupture simulations. Our scenarios incorporate state-of-the-art 3D velocity structure, fault complexity, bathymetry, topography, off-fault plasticity, and viscoelastic attenuation. We vary the segmented fault system geometry and potential hypocenter location in a suite of earthquake scenarios, which vary in terms of earthquake magnitude, fault slip, and the spatio-temporal evolution of rupture dynamics. We find highly variable ground motions, which differ spatially and across scenarios. We consider three fault system geometries of different complexity. All three fault geometries are able to spontaneously produce fully dynamic earthquake scenarios matching historic magnitudes when combined with observationally constrained tectonic background stress and depth-dependent loading. The most complex fault system, Model-A, consists of 55 vertical faults of varying sizes and orientations which are separated by gaps of differing width. This highly segmented geometry does not allow to model dynamically viable and realistic $M_{\mathrm{w}}7+$ scenarios. Our Model-A scenarios feature highly complex rupture dynamics, including branching, dynamic triggering and reverse slip, but rupture only parts of the HFFZ.

The less segmented Model-B and Model-C fault geometries can host sustained dynamic rupture along the well-connected main fault segments. The open gap in Model-B acts as a strong barrier preventing dynamic triggering (rupture jumping), leading to scenarios with magnitudes up to $M_{\mathrm{w}}7.15$. Model-C can host rupture scenarios up to $M_{\mathrm{w}}7.3$ and the complete main fault breaks. Fault roughness can significantly affect rupture dynamics and physically plausible maximum magnitude by either delaying or arresting rupture propagation.

All simulated scenarios yield heterogeneous ground motion distributions. We observe ground shaking amplification from rupture directivity, from localized geometric complexities, such as fault gaps and bends, and from topography. The coupled effects of rupture directivity and fault geometry generate narrow bands with amplified ground motions. Among all simulated scenarios, the strongest ground motion at Húsavík town is SA[1.0s]=$\sim$1.55 g. The physics-based ground motion we generate (quantified by SA[1.0s]) shows good agreement in terms of attenuation relationship with recent ground motion models generated for the SISZ. The ground shaking spatial distribution varies significantly between different rupture scenarios. However, the derived ground motion attenuation relationships for similar magnitude events are nearly identical on average, especially close to the fault. We show that the modeled ground motion variability changes with distance to the fault. It has higher values in unilateral than in bilateral rupture scenarios. Variability is in all simulations on average higher than the typical (constant) standard variation assumed in GMMs. Our synthetic ground motion attenuation relationships are magnitude consistent when breaking the same fault segments. This suggests that fault geometry complexities and dynamic effects such as rupture directivity that change ground motions locally can be captured in unified physics-based GMMs. We conclude that ensembles of physics-based, observationally informed earthquake scenarios can complement empirical seismic hazard assessment methods to better characterize the hazard of tectonically and seismically complex regions, such as the HFFZ in Northern Iceland, especially when historical data are limited and the attenuation relationships are poorly constrained.

## Acknowledgments

We use the open-source software package SeisSol, available at `https://github.com/SeisSol/SeisSol`. Input files required to run all dynamic rupture simulations shown in the study can be downloaded from `https://github.com/Bo-Li-LMU/ChEESE_PSHA`. The

structural model incorporates topography and bathymetry data from GeoMapApp (`www.geomapapp.org`)/(Ryan et al., 2009).

This work received funding from the European Union's Horizon 2020 research and innovation programme (ChEESE, grant agreement No. 823844, TEAR ERC Starting grant agreement No. 852992, DT-Geo grant agreement No. 101058129, Geo-Inquire grant agreement No. 101058518). We acknowledge additional funding from the German Research Foundation (DFG, GA 2465/2-1, GA 2465/3-1), NSF (EAR-2121666) and SCEC (awards 20046, 21010), and the Icelandic Research Fund (SENSHAZ, Grant No. 196089) and King Abdullah University of Science and Technology (KAUST, Grant BAS/1/1339- 01-01).

The authors acknowledge the Gauss Centre for Supercomputing e.V. (www.gauss-centre.eu, project pr63qo) for funding this project by providing computing time on the GCS Supercomputer SuperMUC-NG at Leibniz Supercomputing Centre (www.lrz.de). Computing resources were also provided by the Institute of Geophysics of LMU Munich (Oeser et al., 2006).

## References

Abrahamson, N. A., & Shedlock, K. M. (1997). Overview, seism. *Res. Lett*, *68*(1), 9–23.

Abril, C., Gudmundsson, O., & the SIL seismological group. (2018). Relocating earthquakes with empirical traveltimes. *Geophysical Journal International*, *214*(3), 2098–2114.

Abril, C., Guðmundsson, O., Tryggvason, A., & the SIL seismological group. (2019). Earthquake relocation in the Tjörnes Fracture Zone. In *Proceedings of the International Workshop on Earthquakes in North Iceland.* Húsavík, Iceland.

Abril, C., Tryggvason, A., Gudmundsson, Ó., & Steffen, R. (2021). Local earthquake tomography in the tjörnes fracture zone (north iceland). *Journal of Geophysical Research: Solid Earth*, *126*.

Ando, R., & Kaneko, Y. (2018). Dynamic rupture simulation reproduces spontaneous multifault rupture and arrest during the 2016 mw 7.9 kaikoura earthquake. *Geophysical Research Letters*, *45*(23), 12,875-12,883. Retrieved from `https://agupubs.onlinelibrary.wiley.com/doi/abs/10.1029/2018GL080550` doi: https://doi.org/10.1029/2018GL080550

Andrews, D. (1976). Rupture velocity of plane strain shear cracks. *Journal of Geophysical Research*, *81*(32), 5679–5687.

Andrews, D. (2005). Rupture dynamics with energy loss outside the slip zone. *Journal of Geophysical Research: Solid Earth*, *110*(B1).

Angelier, J., Slunga, R., Bergerat, F., Stefansson, R., & Homberg, C. (2004). Perturbation of stress and oceanic rift extension across transform faults shown by earthquake focal mechanisms in iceland. *Earth and Planetary Science Letters*, *219*(3-4), 271–284.

Aochi, H., & Madariaga, R. (2003). The 1999 izmit, turkey, earthquake: Nonplanar fault structure, dynamic rupture process, and strong ground motion. *Bulletin of the Seismological Society of America*, *93*(3), 1249–1266.

Árnadóttir, T., Lund, B., Jiang, W., Geirsson, H., Björnsson, H., Einarsson, P., & Sigurdsson, T. (2009). Glacial rebound and plate spreading: results from the first countrywide gps observations in iceland. *Geophysical Journal International*, *177*(2), 691–716.

Atik, L. A., Abrahamson, N., Bommer, J. J., Scherbaum, F., Cotton, F., & Kuehn, N. (2010). The variability of ground-motion prediction models and its components. *Seismological Research Letters*, *81*(5), 794–801.

Bai, K., & Ampuero, J.-P. (2017). Effect of seismogenic depth and background stress on physical limits of earthquake rupture across fault step overs. *Journal of Geo-*

*physical Research: Solid Earth*, *122*(12), 10–280.

Ben-Zion, Y., & Sammis, C. G. (2003). Characterization of fault zones. *Pure and applied geophysics*, *160*(3), 677–715.

Bernard, P., & Madariaga, R. (1984). A new asymptotic method for the modeling of near-field accelerograms. *Bulletin of the Seismological Society of America*, *74*(2), 539–557.

Beroza, G. C., & Spudich, P. (1988). Linearized inversion for fault rupture behavior: Application to the 1984 morgan hill, california, earthquake. *Journal of Geophysical Research: Solid Earth*, *93*(B6), 6275–6296.

Biemiller, J., Gabriel, A.-A., & Ulrich, T. (2022). The dynamics of unlikely slip: 3d modeling of low-angle normal fault rupture at the mai'iu fault, papua new guinea. *Geochemistry, Geophysics, Geosystems*, e2021GC010298.

Bistacchi, A., Griffith, W. A., Smith, S. A., Di Toro, G., Jones, R., & Nielsen, S. (2011). Fault roughness at seismogenic depths from lidar and photogrammetric analysis. *Pure and Applied Geophysics*, *168*(12), 2345–2363.

Bommer, J. J., & Stafford, P. J. (2020). Selecting ground-motion models for site-specific psha: Adaptability versus applicability. *Bulletin of the Seismological Society of America*, *110*(6), 2801–2815.

Boore, D. M., & Atkinson, G. M. (2008). Ground-motion prediction equations for the average horizontal component of pga, pgv, and 5%-damped psa at spectral periods between 0.01 s and 10.0 s. *Earthquake Spectra*, *24*(1), 99–138.

Boore, D. M., Watson-Lamprey, J., & Abrahamson, N. A. (2006). Orientation-independent measures of ground motion. *Bulletin of the seismological Society of America*, *96*(4A), 1502–1511.

Brandsdóttir, B., Riedel, C., Richter, B., Helgadóttir, G., Kjartansson, E., Detrick, R., ... Driscoll, N. (2005). Multibeam bathymetric maps of the kolbeinsey ridge and tjörnes fracture zone, n-iceland. *EGU General Assembly*.

Bruhat, L., Klinger, Y., Vallage, A., & Dunham, E. M. (2020). Influence of fault roughness on surface displacement: From numerical simulations to coseismic slip distributions. *Geophysical Journal International*, *220*(3), 1857–1877.

Byerlee, J. (1978). Friction of rocks. In *Rock friction and earthquake prediction* (pp. 615–626). Springer.

Candela, T., Renard, F., Bouchon, M., Brouste, A., Marsan, D., Schmittbuhl, J., & Voisin, C. (2009). Characterization of fault roughness at various scales: Implications of three-dimensional high resolution topography measurements. In *Mechanics, structure and evolution of fault zones* (pp. 1817–1851). Springer.

Chen, K., Feng, W., Liu, Z., & Song, Y. T. (2018). 2017 mw 8.1 tehuantepec earthquake: Deep slip and rupture directivity enhance ground shaking but weaken the tsunami. *Seismological Research Letters*, *89*(4), 1314–1322.

Cotton, F., Scherbaum, F., Bommer, J. J., & Bungum, H. (2006). Criteria for selecting and adjusting ground-motion models for specific target regions: Application to central europe and rock sites. *Journal of Seismology*, *10*(2), 137–156.

Day, S. M., Dalguer, L. A., Lapusta, N., & Liu, Y. (2005). Comparison of finite difference and boundary integral solutions to three-dimensional spontaneous rupture. *Journal of Geophysical Research: Solid Earth*, *110*(B12).

Dieterich, J. H., & Smith, D. E. (2009). Nonplanar faults: Mechanics of slip and off-fault damage. In *Mechanics, structure and evolution of fault zones* (pp. 1799–1815). Springer.

Di Toro, G., Han, R., Hirose, T., De Paola, N., Nielsen, S., Mizoguchi, K., ... Shimamoto, T. (2011). Fault lubrication during earthquakes. *Nature*, *471*(7339), 494–498.

Duan, B. (2008). Asymmetric off-fault damage generated by bilateral ruptures along a bimaterial interface. *Geophysical Research Letters*, *35*(14).

Duan, B., & Oglesby, D. D. (2006). Heterogeneous fault stresses from previous

earthquakes and the effect on dynamics of parallel strike-slip faults. *Journal of Geophysical Research: Solid Earth*, *111*(B5).

Dunham, E. M. (2005). Dissipative interface waves and the transient response of a three-dimensional sliding interface with coulomb friction. *Journal of the Mechanics and Physics of Solids*, *53*(2), 327–357.

Dunham, E. M., Belanger, D., Cong, L., & Kozdon, J. E. (2011). Earthquake ruptures with strongly rate-weakening friction and off-fault plasticity, part 2: Nonplanar faults. *Bulletin of the Seismological Society of America*, *101*(5), 2308–2322.

D'Amico, V., Albarello, D., Sigbjörnsson, R., & Rupakhety, R. (2016). Seismic hazard assessment for iceland in terms of macroseismic intensity using a site approach. *Bulletin of Earthquake Engineering*, *14*(7), 1797–1811.

Einarsson, P. (1991). Earthquakes and present-day tectonism in iceland. *Tectonophysics*, *189*(1-4), 261–279.

Einarsson, P. (2008). Plate boundaries, rifts and transforms in iceland. *Jökull*, *58*(12), 35–58.

Elliott, A., Dolan, J., & Oglesby, D. (2009). Evidence from coseismic slip gradients for dynamic control on rupture propagation and arrest through stepovers. *Journal of Geophysical Research: Solid Earth*, *114*(B2).

Fang, Z., & Dunham, E. M. (2013). Additional shear resistance from fault roughness and stress levels on geometrically complex faults. *Journal of Geophysical Research: Solid Earth*, *118*(7), 3642–3654.

Field, E. H., Jordan, T. H., & Cornell, C. A. (2003). Opensha: A developing community-modeling environment for seismic hazard analysis. *Seismological Research Letters*, *74*(4), 406–419.

Fliss, S., Bhat, H. S., Dmowska, R., & Rice, J. R. (2005). Fault branching and rupture directivity. *Journal of Geophysical Research: Solid Earth*, *110*(B6).

Flóvenz, Ó. G., & Saemundsson, K. (1993). Heat flow and geothermal processes in iceland. *Tectonophysics*, *225*(1-2), 123–138.

Gabriel, A.-A., Ampuero, J.-P., Dalguer, L., & Mai, P. M. (2013). Source properties of dynamic rupture pulses with off-fault plasticity. *Journal of Geophysical Research: Solid Earth*, *118*(8), 4117–4126.

Gallovič, F., Valentová, L., Ampuero, J.-P., & Gabriel, A.-A. (2019). Bayesian dynamic finite-fault inversion: 2. application to the 2016 mw 6.2 amatrice, italy, earthquake. *Journal of Geophysical Research: Solid Earth*, *124*(7), 6970–6988.

Galvez, P., Somerville, P., Petukhin, A., Ampuero, J.-P., & Peter, D. (2020). Earthquake cycle modelling of multi-segmented faults: Dynamic rupture and ground motion simulation of the 1992 mw 7.3 landers earthquake. *Pure and Applied Geophysics*, *177*(5), 2163–2179.

Graves, R., Jordan, T. H., Callaghan, S., Deelman, E., Field, E., Juve, G., ... others (2011). Cybershake: A physics-based seismic hazard model for southern california. *Pure and Applied Geophysics*, *168*(3), 367–381.

Graves, R., & Pitarka, A. (2016). Kinematic ground-motion simulations on rough faults including effects of 3d stochastic velocity perturbations. *Bulletin of the Seismological Society of America*, *106*(5), 2136–2153.

Guatteri, M., Mai, P. M., & Beroza, G. C. (2004). A pseudo-dynamic approximation to dynamic rupture models for strong ground motion prediction. *Bulletin of the Seismological Society of America*, *94*(6), 2051–2063.

Guatteri, M., Mai, P. M., Beroza, G. C., & Boatwright, J. (2003). Strong ground-motion prediction from stochastic-dynamic source models. *Bulletin of the Seismological Society of America*, *93*(1), 301–313.

Halldórsson, B. (2019). Towards improved seismic monitoring, earthquake modeling and ground motion simulation for early warning and hazard estimates in north iceland. In *proceedings of the northquake 2019 workshop, edited by sigurjón jónsson and benedikt halldórsson and kristín jónsdóttir and páll einarsson*

*and ragnar stefánsson and helena eydís ingólfsdóttir and heiða elín aðalsteinsdóttir* (p. 124-127). Retrieved from `https://hac.is/wp-content/uploads/Northquake2019.pdf` (Husavik, North Iceland, 21-24 May 2019)

Harris, R. A., Barall, M., Aagaard, B., Ma, S., Roten, D., Olsen, K., ... others (2018). A suite of exercises for verifying dynamic earthquake rupture codes. *Seismological Research Letters*, *89*(3), 1146–1162.

Harris, R. A., Barall, M., Andrews, D. J., Duan, B., Ma, S., Dunham, E. M., ... others (2011). Verifying a computational method for predicting extreme ground motion. *Seismological Research Letters*, *82*(5), 638–644.

Hensch, M., Guðmundsson, G., & the SIL monitoring group. (2013). Offshore seismicity with large azimuthal gaps: Challenges for the SIL network. In *Proceedings of the International Workshop on Earthquakes in North Iceland.* Húsavík, Iceland.

Hjartardóttir, Á., Einarsson, P., Magnúsdóttir, S., Björnsdóttir, Þ., & Brandsdóttir, B. (2016). Fracture systems of the northern volcanic rift zone, iceland: an onshore part of the mid-atlantic plate boundary. *Geological Society, London, Special Publications*, *420*(1), 297–314.

Huang, Y., & Ampuero, J.-P. (2011). Pulse-like ruptures induced by low-velocity fault zones. *Journal of Geophysical Research: Solid Earth*, *116*(B12).

Ida, Y. (1972). Cohesive force across the tip of a longitudinal-shear crack and griffith's specific surface energy. *Journal of Geophysical Research*, *77*(20), 3796–3805.

Idini, B., & Ampuero, J.-P. (2020). Fault-zone damage promotes pulse-like rupture and back-propagating fronts via quasi-static effects. *Geophysical Research Letters*, *47*(23), e2020GL090736.

Käser, M., Hermann, V., & Puente, J. d. l. (2008). Quantitative accuracy analysis of the discontinuous galerkin method for seismic wave propagation. *Geophysical Journal International*, *173*(3), 990–999.

Kowsari, M., Sonnemann, T., Halldorsson, B., Hrafnkelsson, B., Snæbjörnsson, J. Þ., & Jonsson, S. (2020). Bayesian inference of empirical ground motion models to pseudo-spectral accelerations of south iceland seismic zone earthquakes based on informative priors. *Soil Dynamics and Earthquake Engineering*, *132*, 106075.

Kurzon, I., Vernon, F. L., Ben-Zion, Y., & Atkinson, G. (2014). Ground motion prediction equations in the san jacinto fault zone: Significant effects of rupture directivity and fault zone amplification. *Pure and Applied Geophysics*, *171*(11), 3045–3081.

Kyriakopoulos, C., Oglesby, D., Rockwell, T., Meltzner, A., Barall, M., Fletcher, J. M., & Tulanowski, D. (2019). Dynamic rupture scenarios in the brawley seismic zone, salton trough, southern california. *Journal of Geophysical Research: Solid Earth*, *124*(4), 3680–3707.

Li, B., Wu, B., Bao, H., Oglesby, D. D., Ghosh, A., Gabriel, A.-A., ... Chu, R. (2022). Rupture heterogeneity and directivity effects in back-projection analysis. *Journal of Geophysical Research: Solid Earth*, *127*(3), e2021JB022663.

Liu, D., Duan, B., Prush, V. B., Oskin, M. E., & Liu-Zeng, J. (2021). Observation-constrained multicycle dynamic models of the pingding shan earthquake gate along the altyn tagh fault. *Tectonophysics*, *814*, 228948.

Liu, D., Duan, B., Scharer, K., & Yule, D. (2022). Observation-constrained multicycle dynamic models of the southern san andreas and the northern san jacinto faults: Addressing complexity in paleoearthquake extent and recurrence with realistic 2d fault geometry. *Journal of Geophysical Research: Solid Earth*, *127*(2), e2021JB023420.

Lozos, J. C. (2016). A case for historic joint rupture of the san andreas and san jacinto faults. *Science advances*, *2*(3), e1500621.

Madden, E. H., Ulrich, T., & Gabriel, A.-A. (2022). The state of pore fluid pressure and 3-d megathrust earthquake dynamics. *Journal of Geophysical Research: Solid Earth*, *127*(4), e2021JB023382.

Magnúsdóttir, S., Brandsdóttir, B., Driscoll, N., & Detrick, R. (2015). Postglacial tectonic activity within the skjálfandadjúp basin, tjörnes fracture zone, offshore northern iceland, based on high resolution seismic stratigraphy. *Marine Geology*, *367*, 159–170.

Magnúsdóttir, S., & Brandsdóttir, B. (2011). Tectonics of the Þeistareykir fissure swarm. *Jökull*, *61*, 65–79.

Mai, P., & Beroza, G. (2000). Source scaling properties from finite-fault-rupture models. *Bulletin of the Seismological Society of America*, *90*(3), 604–615.

Mai, P. M., Schorlemmer, D., Page, M., Ampuero, J.-P., Asano, K., Causse, M., ... others (2016). The earthquake-source inversion validation (siv) project. *Seismological Research Letters*, *87*(3), 690–708.

Mai, P. M., Spudich, P., & Boatwright, J. (2005). Hypocenter locations in finite-source rupture models. *Bulletin of the Seismological Society of America*, *95*(3), 965–980.

Mavroeidis, G. P., & Papageorgiou, A. S. (2003). A mathematical representation of near-fault ground motions. *Bulletin of the seismological society of America*, *93*(3), 1099–1131.

Metzger, S., & Jónsson, S. (2014). Plate boundary deformation in north iceland during 1992–2009 revealed by insar time-series analysis and gps. *Tectonophysics*, *634*, 127–138.

Metzger, S., Jónsson, S., & Geirsson, H. (2011). Locking depth and slip-rate of the húsavík flatey fault, north iceland, derived from continuous gps data 2006-2010. *Geophysical Journal International*, *187*(2), 564–576.

Morris, A., Ferrill, D. A., & Henderson, D. B. (1996). Slip-tendency analysis and fault reactivation. *Geology*, *24*(3), 275–278.

Nekrasova, A., Kossobokov, V., Peresan, A., & Magrin, A. (2014). The comparison of the ndsha, psha seismic hazard maps and real seismicity for the italian territory. *Natural Hazards*, *70*(1), 629–641.

Oeser, J., Bunge, H.-P., & Mohr, M. (2006). Cluster design in the earth sciences tethys. In *International conference on high performance computing and communications* (pp. 31–40).

Oglesby, D. D. (2005). The dynamics of strike-slip step-overs with linking dip-slip faults. *Bulletin of the Seismological Society of America*, *95*(5), 1604–1622.

Oglesby, D. D. (2020). What can surface-slip distributions tell us about fault connectivity at depth? *Bulletin of the Seismological Society of America*, *110*(3), 1025–1036.

Oglesby, D. D., & Mai, P. M. (2012). Fault geometry, rupture dynamics and ground motion from potential earthquakes on the north anatolian fault under the sea of marmara. *Geophysical Journal International*, *188*(3), 1071–1087.

Olsen, K., Day, S., Dalguer, L., Mayhew, J., Cui, Y., Zhu, J., ... others (2009). Shakeout-d: Ground motion estimates using an ensemble of large earthquakes on the southern san andreas fault with spontaneous rupture propagation. *Geophysical Research Letters*, *36*(4).

Pacor, F., Gallovič, F., Puglia, R., Luzi, L., & D'Amico, M. (2016, May). Diminishing high-frequency directivity due to a source effect: Empirical evidence from small earthquakes in the Abruzzo region, Italy. *Geophysical Research Letters*, *43*(10), 5000–5008. (Publisher: John Wiley & Sons, Ltd) doi: 10.1002/2016GL068546

Palgunadi, K. H., Gabriel, A.-A., Ulrich, T., López-Comino, J. Á., & Mai, P. M. (2020). Dynamic fault interaction during a fluid-injection-induced earthquake: The 2017 m w 5.5 pohang event. *Bulletin of the Seismological Society of America*, *110*(5), 2328–2349.

Panzera, F., Zechar, J. D., Vogfjörd, K. S., & Eberhard, D. A. (2016). A revised earthquake catalogue for south iceland. *Pure and Applied Geophysics*, *173*(1), 97–

116.

Passarelli, L., Rivalta, E., Jónsson, S., Hensch, M., Metzger, S., Jakobsdóttir, S. S., ... Dahm, T. (2018). Scaling and spatial complementarity of tectonic earthquake swarms. *Earth and Planetary Science Letters*, *482*, 62–70.

Pelties, C., Gabriel, A.-A., & Ampuero, J.-P. (2014). Verification of an ader-dg method for complex dynamic rupture problems. *Geoscientific Model Development*, *7*(3), 847–866.

Poliakov, A. N., Dmowska, R., & Rice, J. R. (2002). Dynamic shear rupture interactions with fault bends and off-axis secondary faulting. *Journal of Geophysical Research: Solid Earth*, *107*(B11), ESE–6.

Power, W. L., & Tullis, T. E. (1991). Euclidean and fractal models for the description of rock surface roughness. *Journal of Geophysical Research: Solid Earth*, *96*(B1), 415–424.

Rodgers, A. J., Pitarka, A., Pankajakshan, R., Sjögreen, B., & Petersson, N. A. (2020). Regional-scale 3d ground-motion simulations of mw 7 earthquakes on the hayward fault, northern california resolving frequencies 0–10 hz and including site-response corrections. *Bulletin of the Seismological Society of America*, *110*(6), 2862–2881.

Rögnvaldsson, S. T., Gudmundsson, A., & Slunga, R. (1998). Seismotectonic analysis of the tjörnes fracture zone, an active transform fault in north iceland. *Journal of Geophysical Research: Solid Earth*, *103*(B12), 30117–30129.

Roten, D., Olsen, K., & Day, S. (2017). Off-fault deformations and shallow slip deficit from dynamic rupture simulations with fault zone plasticity. *Geophysical Research Letters*, *44*(15), 7733–7742.

Roten, D., Olsen, K., Day, S., Cui, Y., & Fäh, D. (2014). Expected seismic shaking in los angeles reduced by san andreas fault zone plasticity. *Geophysical Research Letters*, *41*(8), 2769–2777.

Roten, D., Olsen, K., & Pechmann, J. (2012). 3d simulations of m 7 earthquakes on the wasatch fault, utah, part ii: Broadband (0–10 hz) ground motions and nonlinear soil behavior. *Bulletin of the Seismological Society of America*, *102*(5), 2008–2030.

Ryan, W. B., Carbotte, S. M., Coplan, J. O., O'Hara, S., Melkonian, A., Arko, R., ... others (2009). Global multi-resolution topography synthesis. *Geochemistry, Geophysics, Geosystems*, *10*(3).

Sagy, A., Brodsky, E. E., & Axen, G. J. (2007). Evolution of fault-surface roughness with slip. *Geology*, *35*(3), 283–286.

Savran, W., & Olsen, K. (2020). Kinematic rupture generator based on 3-d spontaneous rupture simulations along geometrically rough faults. *Journal of Geophysical Research: Solid Earth*, *125*(10), e2020JB019464.

Schmedes, J., Archuleta, R. J., & Lavallée, D. (2010). Correlation of earthquake source parameters inferred from dynamic rupture simulations. *Journal of Geophysical Research: Solid Earth*, *115*(B3).

Scholz, C., Dawers, N., Yu, J.-Z., Anders, M., & Cowie, P. (1993). Fault growth and fault scaling laws: Preliminary results. *Journal of Geophysical Research: Solid Earth*, *98*(B12), 21951–21961.

Shi, Z., & Day, S. M. (2013). Rupture dynamics and ground motion from 3-d rough-fault simulations. *Journal of Geophysical Research: Solid Earth*, *118*(3), 1122–1141.

Silva, V., Amo-Oduro, D., Calderon, A., Costa, C., Dabbeek, J., Despotaki, V., ... others (2020). Development of a global seismic risk model. *Earthquake Spectra*, *36*(1_suppl), 372–394.

Smith-Konter, B., & Sandwell, D. (2009). Stress evolution of the san andreas fault system: Recurrence interval versus locking depth. *Geophysical Research Letters*, *36*(13).

Snaebjornsson, J., & Sigbjornsson, R. (2007). *Earthquake action in geothermal projects in ne iceland at krafla, bjarnarflag, gjastykki and theistareykir: assessment of geohazards affecting energy production and transmission systems emphasizing structural design criteria and mitigation of risk. theistareykir ltd, landsnet, landsvirkjun* (Tech. Rep.). report no. LV-2007/075.

Solnes, J., Sigbjörnsson, R., & Eliasson, J. (2004). Probabilistic seismic hazard mapping of iceland. In *Proceedings of the 13th world conference on earthquake engineering, vancouver, bc, canada.*

Somerville, P., & Graves, R. (1993). Conditions that give rise to unusually large long period ground motions. *The structural design of tall buildings*, *2*(3), 211–232.

Somerville, P. G., Smith, N. F., Graves, R. W., & Abrahamson, N. A. (1997). Modification of empirical strong ground motion attenuation relations to include the amplitude and duration effects of rupture directivity. *Seismological research letters*, *68*(1), 199–222.

Spudich, P., & Frazer, L. N. (1984). Use of ray theory to calculate high-frequency radiation from earthquake sources having spatially variable rupture velocity and stress drop. *Bulletin of the Seismological Society of America*, *74*(6), 2061–2082.

Stefansson, R., Gudmundsson, G. B., & Halldorsson, P. (2008). Tjörnes fracture zone. new and old seismic evidences for the link between the north iceland rift zone and the mid-atlantic ridge. *Tectonophysics*, *447*(1-4), 117–126.

Strasser, F. O., Abrahamson, N. A., & Bommer, J. J. (2009). Sigma: Issues, insights, and challenges. *Seismological Research Letters*, *80*(1), 40–56.

Taufiqurrahman, T., Gabriel, A.-A., Ulrich, T., Valentova, L., & Gallovič, F. (2022). Broadband dynamic rupture modeling with fractal fault roughness, frictional heterogeneity, viscoelasticity and topography: the 2016 mw 6.2 amatrice, italy earthquake. *Earth and Space Science Open Archive*, 31. Retrieved from `https://doi.org/10.1002/essoar.10510965.1` doi: 10.1002/essoar.10510965.1

Templeton, E. L., & Rice, J. R. (2008). Off-fault plasticity and earthquake rupture dynamics: 1. dry materials or neglect of fluid pressure changes. *Journal of Geophysical Research: Solid Earth*, *113*(B9).

Tinti, E., Casarotti, E., Ulrich, T., Taufiqurrahman, T., Li, D., & Gabriel, A.-A. (2021). Constraining families of dynamic models using geological, geodetic and strong ground motion data: The mw 6.5, october 30th, 2016, norcia earthquake, italy. *Earth and Planetary Science Letters*, *576*, 117237.

Ulrich, T., Gabriel, A.-A., Ampuero, J.-P., & Xu, W. (2019). Dynamic viability of the 2016 mw 7.8 kaikōura earthquake cascade on weak crustal faults. *Nature communications*, *10*(1), 1–16.

Ulrich, T., Gabriel, A.-A., & Madden, E. H. (2022). Stress, rigidity and sediment strength control megathrust earthquake and tsunami dynamics. *Nature Geoscience*, *15*(1), 67–73.

Ulrich, T., Vater, S., Madden, E. H., Behrens, J., Dinther, Y. v., Zelst, I. v., ... Gabriel, A.-A. (2019, October). Coupled, Physics-Based Modeling Reveals Earthquake Displacements are Critical to the 2018 Palu, Sulawesi Tsunami. *Pure and Applied Geophysics*, *176*(10), 4069–4109. doi: 10.1007/s00024-019-02290-5

Wang, Y., & Day, S. M. (2020). Effects of off-fault inelasticity on near-fault directivity pulses. *Journal of Geophysical Research: Solid Earth*, *125*(7), e2019JB019074.

Wesnousky, S. G. (1988). Seismological and structural evolution of strike-slip faults. *Nature*, *335*(6188), 340–343.

Withers, K. B., Olsen, K. B., Day, S. M., & Shi, Z. (2019). Ground motion and intraevent variability from 3d deterministic broadband (0–7.5 hz) simulations along a nonplanar strike-slip fault. *Bulletin of the Seismological Society of America*, *109*(1), 229–250.

Wollherr, S., Gabriel, A.-A., & Mai, P. M. (2019). Landers 1992 "reloaded": Integrative dynamic earthquake rupture modeling. *Journal of Geophysical Research:*

*Solid Earth*, *124*(7), 6666–6702.

Wollherr, S., Gabriel, A.-A., & Uphoff, C. (2018). Off-fault plasticity in three-dimensional dynamic rupture simulations using a modal discontinuous galerkin method on unstructured meshes: implementation, verification and application. *Geophysical Journal International*, *214*(3), 1556–1584.

Xu, S., Ben-Zion, Y., & Ampuero, J.-P. (2012). Properties of inelastic yielding zones generated by in-plane dynamic ruptures—i. model description and basic results. *Geophysical Journal International*, *191*(3), 1325–1342.

Ziegler, M., Rajabi, M., Heidbach, O., Hersir, G. P., Ágústsson, K., Árnadóttir, S., & Zang, A. (2016). The stress pattern of iceland. *Tectonophysics*, *674*, 101–113.